Title: Simulations of Two Heavily Confined PBX 9502 Cook-off Experiments.

Author(s): Aviles-Ramos, Cuauhtemoc
Parker, Gary Robert Jr.
Holmes, Matthew David

Intended for: Technical Report

Issued: 2018-03-07

Simulations of Two Heavily Confined PBX 9502 Cook-off Experiments

Aviles–Ramos[†], C., Parker[‡], Jr., G. R., and Holmes[‡], M. D.
Los Alamos National Laboratory, W-13[†], M-6[‡].
Los Alamos, New Mexico 87545

Abstract

Finite element models of two cook-off experiments were constructed using the Aria code [1].These experiments [2] provided thermocouple measurements that were used as boundary conditions to carry out finite element (FE) simulations and comparisons of the FE thermal response with internal temperature measurements in the PBX 9502. These FE models contain a pressure dependent PBX 9502 thermal decomposition model developed by Hobbs' et al. [3]. Comparisons of the FE results and the experiments are presented. These comparisons assess the predictive capabilities of Hobbs' model under the experimental conditions. Limiting cases of the PBX 9502 decomposition model are considered. Two parameterizations associated with the pressure dependency of the PBX 9502 decomposition model were carried out to fit the experiments using internal temperature measurements. Two inverse heat conduction problems were implemented to estimate temperatures as functions of time at locations on the outer surface of the PBX 9502. Thermocouple conduction error studies were carried out to assess the comparisons of the FE model thermal response with the experiments.

Heavily confined tests description

Two heavily confined tests were conducted in September 2014 [2]. The first test, LT-55-1, had a vented configuration, and the second test, LT-55-2, was not vented. Figure 1 shows the heavily confined cook-off design with tubing projected from the top which was open for the vented configuration and sealed by a static pressure transducer for the unvented configuration. Heating
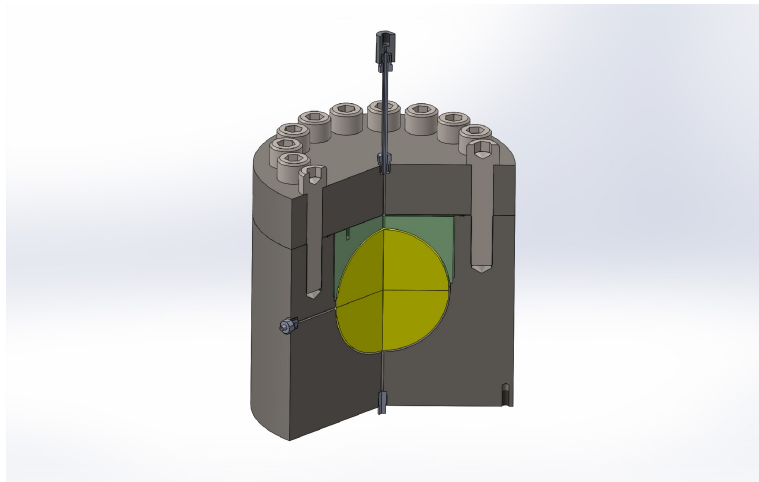

Figure 1. Heavily confined cook-off apparatus showing two yellow PBX 9502 hemispheres, pressure transducer port, and 4340 heat-treated steel confinement vessel.

tapes were wrapped around the lateral surface of the cylindrical confinement which provided the heating profiles for the experiments. A predefined heating profile that consisted of a temperature ramp to 230 °C was applied first. Then, the surface temperature was kept constant at 230 °C until the temperature at the center of the PBX 9502 reached ~230 °C. After this initial ramp, the surface temperature was ramped again to 255 °C and this temperature was kept constant until thermal ignition. Figure 2 shows a picture of the LT-55-1 test
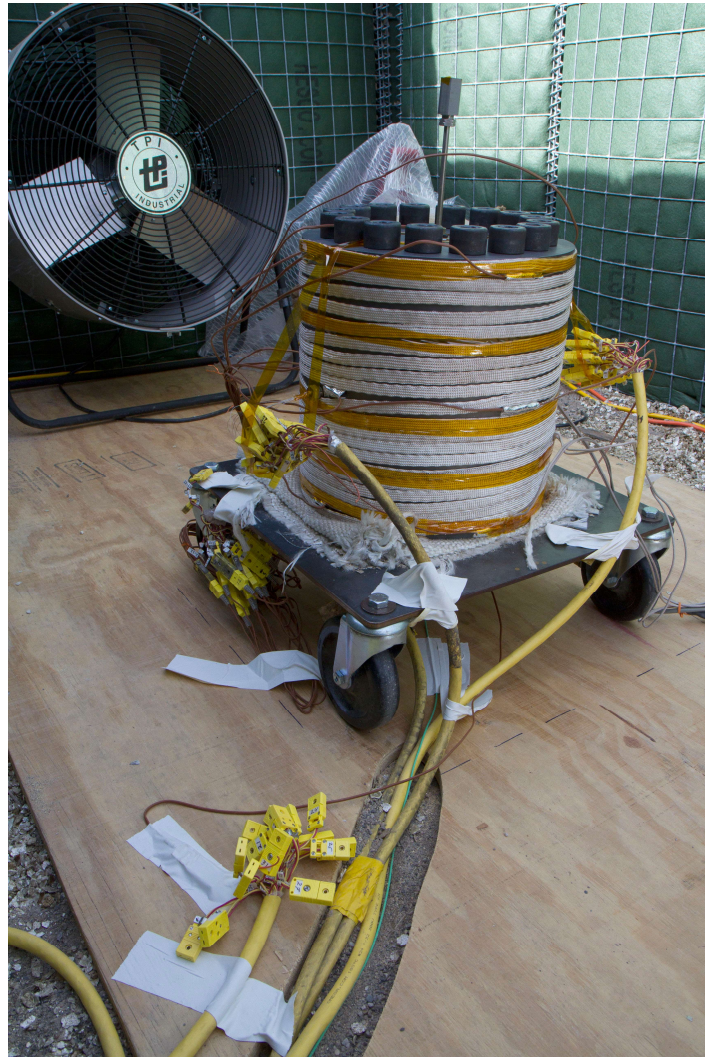

Figure 2. LT-55-1 test setup showing heating tapes, pressure port, base, and thermocouple wires.

The heavily confined PBX 9502 cook-off design consists of two 6" diameter hemispheres of PBX 9502 (~7.75 lb) confined in a 4340 heat-treated steel vessel. Figure 3 shows a sketch of this experimental setup. Figure 4 shows the two PBX 9502 hemispheres and the mid-plane located
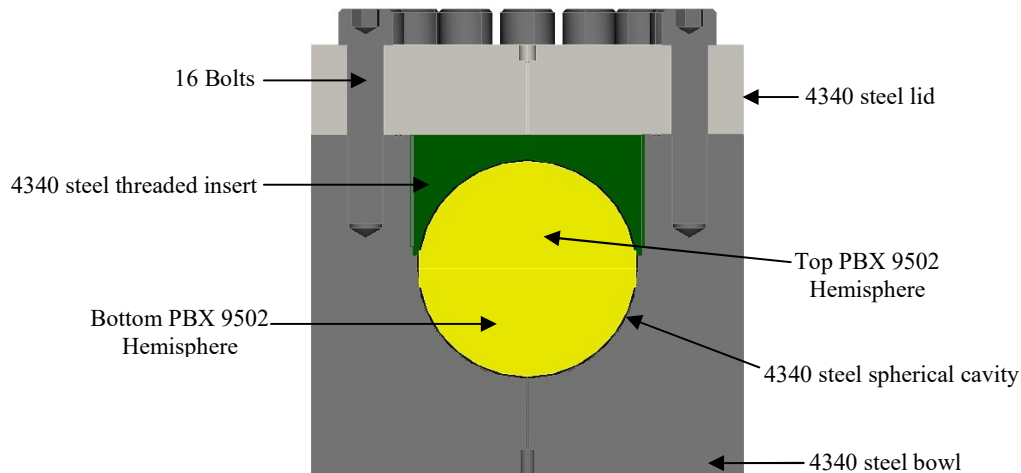
Figure 3. Sketch of heavily confined PBX 9502 cookoff test.
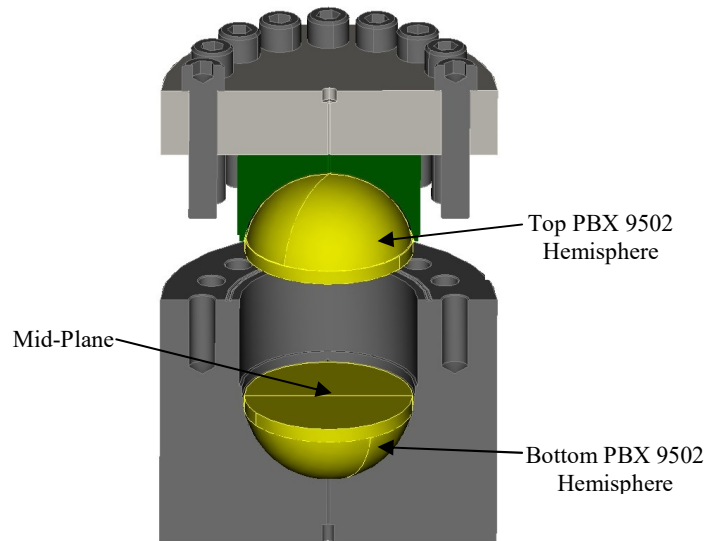
Figure 4. Location of mid-plane where some of the internal thermocouples were installed.

between the PBX 9502 hemispheres. Thermocouples were installed at the interface between the PBX 9502 and the steel, in the mid-plane between the two PBX 9502 hemispheres, and on the outer surfaces of the steel confinement. Sketches for all thermocouples locations are given in Appendix A. Figure 5 shows the location of the thermocouples installed on the outer surfaces of the steel confinement. These thermocouple measurements can be used to define temperature boundary conditions which can be codified to carry out FE simulations of these experiments. Figure 6 and 7 show outer mid-plane thermocouple measurements for the boundary conditions implemented for the LT-55-1 and LT-55-2 experiments respectively. These boundary conditions were carefully planned to get thermal ignition at the center of the PBX 9502 sphere. Figures 6 and 7 also show the temperatures measured at the PBX 9502 center.

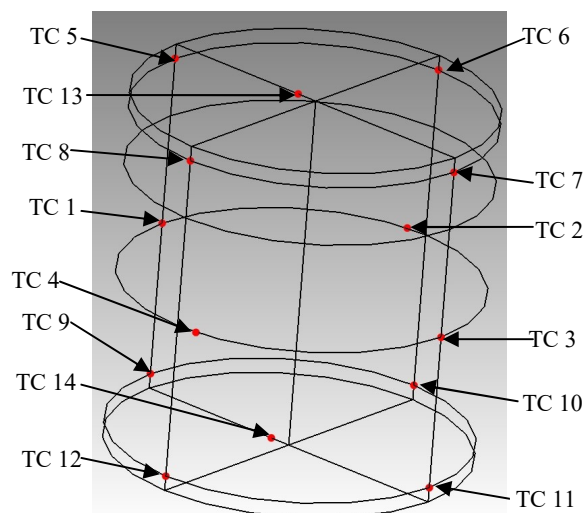Figure 5. Thermocouples installed on the
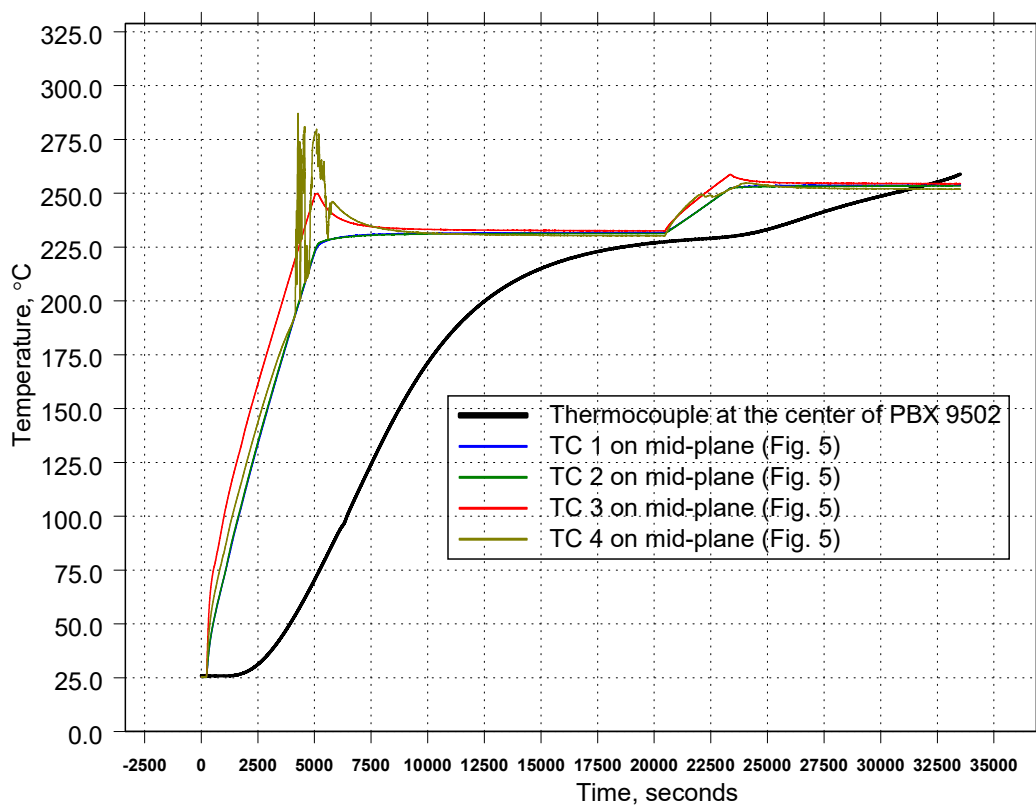outer surface of the steel confinement.

Figure 6. Steel confinement vessel outer mid-plane thermocouples and
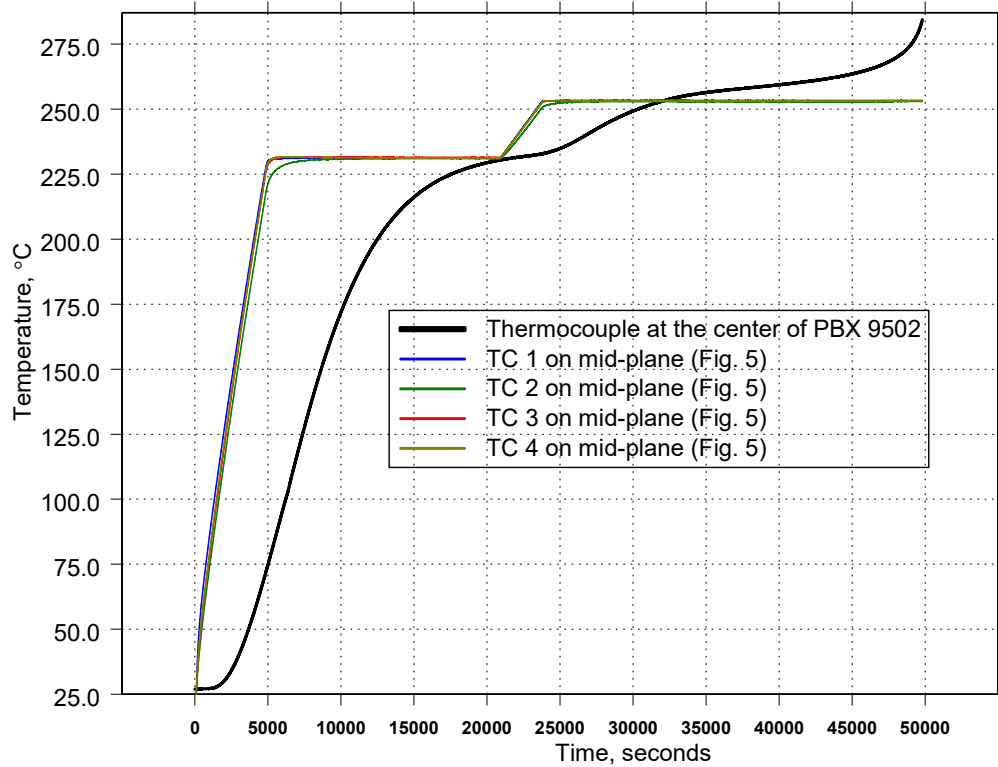and temperatures measured at the center of PBX 9502 for test LT-55-1.

Figure 7. Steel confinement vessel outer mid-plane thermocouples and temperatures measured at the center of PBX 9502 for test LT-55-2.

Temperatures measured by the thermocouples installed at the PBX 9502–steel interface were used to define a temperature boundary condition on the outer surfaces of the PBX 9502 hemispheres. Thermocouples located at the bottom PBX 9502 hemisphere–steel interface were taped to the steel spherical cavity and the thermocouples located at the top PBX 9502 hemisphere–steel interface were taped to the top surface of the PBX 9502 hemisphere. The mid-plane thermocouples were taped to the top surface of the bottom PBX 9502 hemisphere. Figures A1 and A2 show the locations of the thermocouples on the steel bottom spherical cavity and on the top surface of the PBX 9502 hemisphere respectively for test LT-55-1. Also, Figs. A3 and A4 (given in Appendix A) show the locations of the thermocouples on the steel bottom spherical cavity and on the top surface of the PBX 9502 hemisphere respectively for test LT-55-2.

Dynamic pressure was measured in both tests and showed similar peak pressures (~110 kpsi) before confinement failure. Figure 8 shows the dynamic pressure measurements. Static pressure was measured for the LT-55-2 ("sealed") test. Figure 9 shows the static pressure measurements. This figure shows periods where the pressure decreases and eventually increases again. It appears from this data that a leak developed for this test. Reference [2] points out that a likely cause for this leak might have been the imperfect brazing of the wires of the thermocouples located at the PBX 9502 hemisphere–steel interface and at the mid-plane.

The temperature data obtained in these experiments permits to carry out two types of simulations. The first type considers the boundary conditions defined by the thermocouples shown in Fig. 6. The second type uses the thermocouple data measured at the PBX 9502–steel interface to define a temperature boundary condition on the surface of the PBX 9502 sphere.
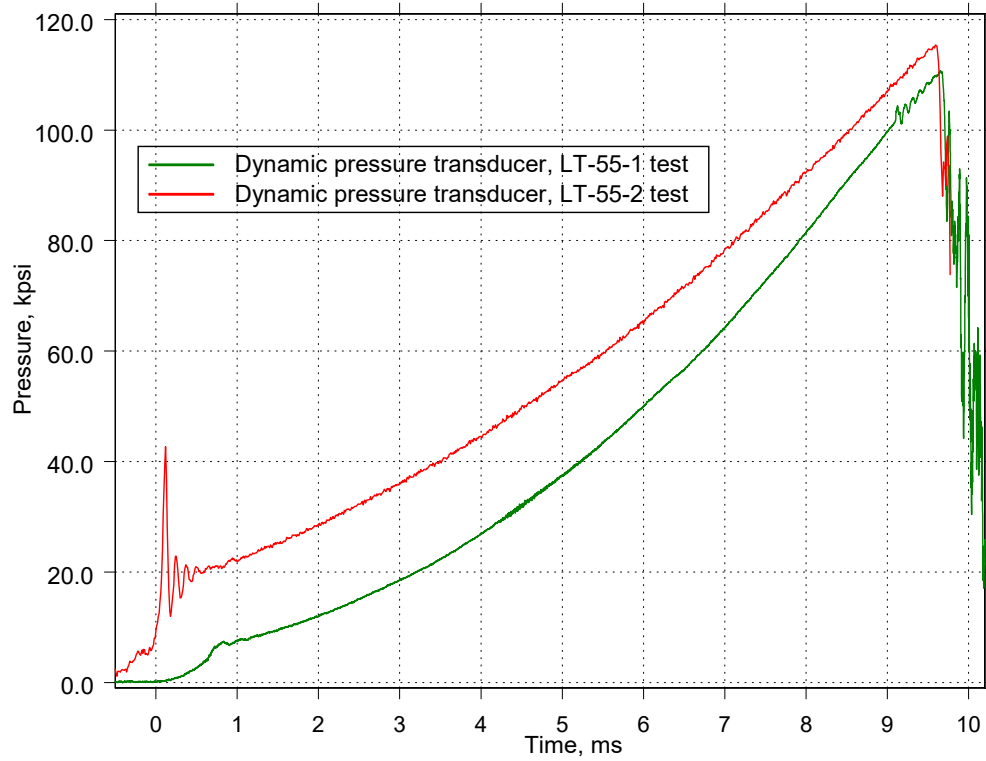
5

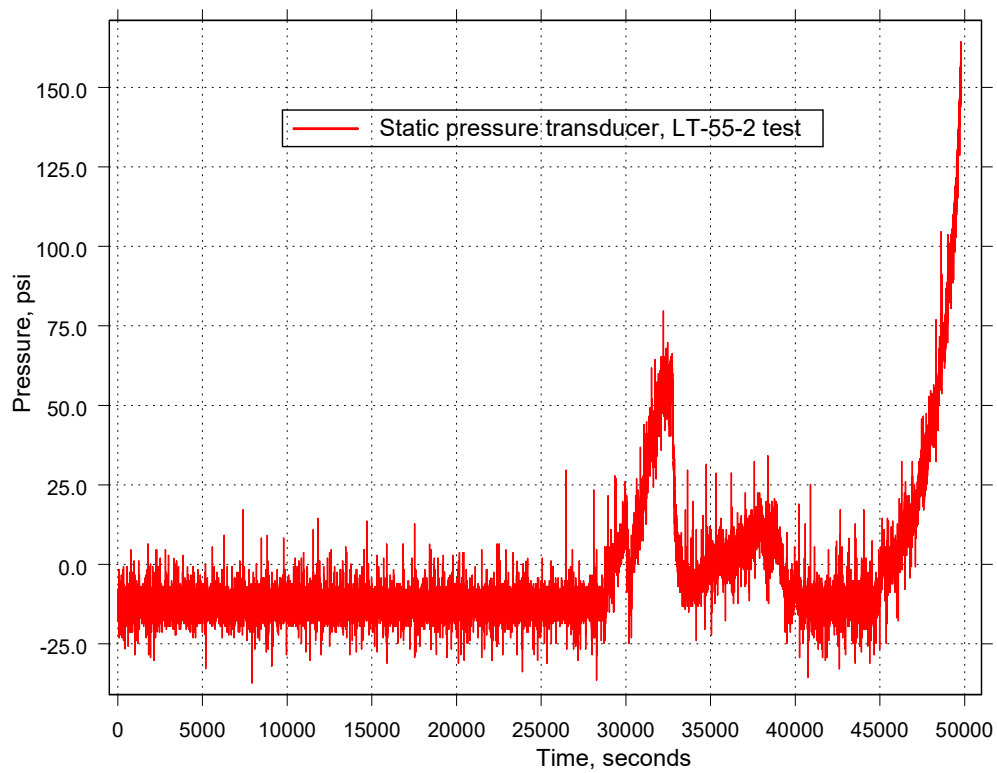Figure 8. Dynamic pressure measured for the LT-55-1 & -2 experiments.

Figure 9. Static pressure measured for the LT-55-2 experiment.

Finite element simulations of test LT-55-1

Simulations that use the thermocouple measurements at the PBX 9502–steel interface as boundary conditions was carried out. This was done to avoid any uncertainties associated with the thermal properties of the steel vessel and the surfaces contact conditions at the PBX 9502–steel interface. The temperatures measured by the thermocouples shown in Figs. A1 and A2 of Appendix A are used to define a temperature boundary condition on the surface of the PBX 9502 sphere. The definition of this boundary condition was done using a C/C++ user plug-in available in the FE code Aria [1]. This user subroutine makes available the Cartesian coordinates of the nodes that define the finite element faces on the outer surface of the PBX 9502 sphere. These coordinates are transformed into spherical using the coordinate system depicted in Fig. 10.
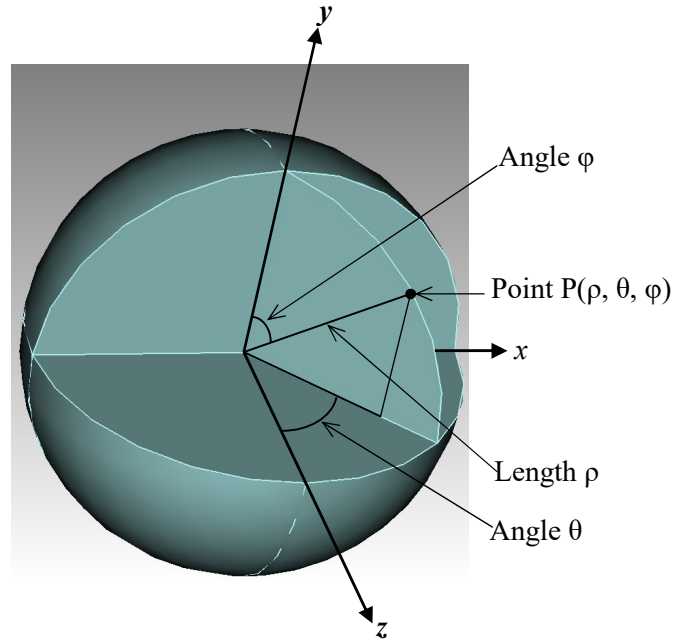
Figure 10. Coordinate system used to calculate the spherical coordinates of the nodes located on the outer surface of the PBX 9502 sphere.

The temperature on the nodes located between the thermocouples shown in Figs. A1 and A2 was calculated assuming the surface temperature is a linear function of the angles θ and φ. For example, assuming that the measured temperatures TC 41, TC 42, and TC 22 in Fig. 11 are represented by $T(\varphi_1)$, $T(\theta_2, \varphi_2)$, and $T(\theta_3, \varphi_2)$ respectively, the temperatures $T(\theta_2, \varphi_4)$, $T(\theta_3, \varphi_4)$, and $T(\theta, \varphi_4)$ shown by block dots in Fig. 11 can be obtained by linear interpolation.

$$T(\theta_2, \varphi_4) = T(\varphi_1) - \left(\frac{\varphi_1 - \varphi_4}{\varphi_1 - \varphi_2} \right) \left[T(\varphi_1) - T(\theta_2, \varphi_2) \right] \qquad (1)$$

$$T(\theta_3, \varphi_4) = T(\varphi_1) - \left(\frac{\varphi_1 - \varphi_4}{\varphi_1 - \varphi_2} \right) \left[T(\varphi_1) - T(\theta_3, \varphi_2) \right] \qquad (2)$$

$$T(\theta,\varphi_4)=T(\theta_2,\varphi_4)-\left(\frac{\theta_2-\theta}{\theta_2-\theta_3}\right)\left[T(\theta_2,\varphi_4)-T(\theta_3,\varphi_4)\right] \qquad (3)$$
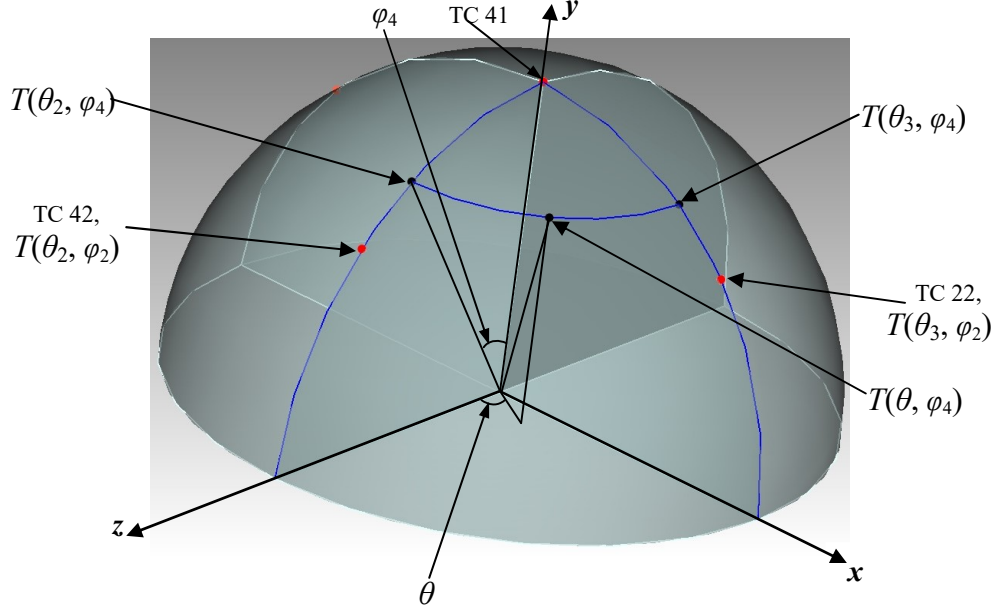
Figure 11. Linear interpolation between thermocouples to find the temperature at a point (θ, φ) on the surface of the PBX 9502 sphere.

Four interpolation schemes were implemented to calculate the nodal surface coordinates on and between the meridians located on the (z, y), $(z, -y)$, (x, y), $(x, -y)$, $(-z, y)$, $(-z, -y)$, $(-x, y)$, and $(-x, -y)$ planes. These schemes were implemented in Aria [1] C/C++ user subroutines. Note that the meridians located on the (z, y) and (x, y) planes are drawn with blue lines in Fig 11. The relationships between the spherical and rectangular coordinate systems shown in Fig. 10 used to calculate the angular coordinates of the FE mesh nodes on the surface of the PBX 9502 sphere are

$$x = \rho\sin(\varphi)\sin(\theta),\; y = \rho\cos(\varphi),\; z = \rho\sin(\varphi)\cos(\theta) \qquad (4)$$

$$\theta = \arctan\left(\frac{x}{z}\right) = \arccos\left(\frac{z}{\sqrt{z^2+x^2}}\right) = \arcsin\left(\frac{x}{\sqrt{z^2+x^2}}\right) \qquad (5)$$

$$\varphi = \arctan\left(\frac{\sqrt{z^2+x^2}}{y}\right) = \arccos\left(\frac{y}{\sqrt{z^2+x^2+y^2}}\right) \qquad (6)$$

for $\rho \geq 0$, $0 \leq \theta \leq 2\pi$, and $0 \leq \varphi \leq \pi$.

The conductive energy equation in the PBX 9502 sphere was used to model this decomposition process. A PBX 9502 pressure dependent thermal decomposition model

8

developed by Hobbs' et al. [3] was used to define a volumetric source term in the PBX 9502 heat conduction equation. This model considers 4 reaction steps in a global mechanism that defines the decomposition of PBX 9502. The first reaction considers drying of the PBX, where the mass fraction of adsorbed water is small. The second reaction involves elimination of a water molecule from TATB to form mono-furazan (MF), which subsequently decomposes into stable reaction products. The final reaction is direct decomposition of TATB to form equilibrium products. The four-step mechanism reads [3],

1. $H_2O_a \rightarrow H_2O_g$

2. $TATB \rightarrow MF + H_2O_m$

3. $MF \rightarrow 6.52\ Gas_m + 4.18\ Carbon_m$

4. $TATB \rightarrow 7.5\ Gas_t + 3.9\ Carbon_t$

where subscript a means adsorbed, subscript g means gaseous, subscript m means coming from the mono-furazan decomposition, and subscript t means coming from the TATB decomposition. The reaction rates associated with the four reaction steps assume first order reactions [3]

$$r_1 = A_1 \exp\left(\frac{-E_1 \pm \xi_1\sigma_1}{RT}\right)\left[H_2O_a\right] \tag{7}$$

$$r_2 = A_2 \exp\left(\frac{-E_2}{RT}\right)\left[TATB\right] \tag{8}$$

$$r_3 = A_3 \exp\left(\frac{-E_3}{RT}\right)\left[MF\right] \tag{9}$$

$$r_4 = A_4 \left(\frac{P}{P_0}\right)^e T^{-3} \exp\left(\frac{-E_4 \pm \xi_4\sigma_4}{RT}\right)\left[TATB\right] \tag{10}$$

where the species concentrations in square brackets [.] are in kgmol/m^3, $e = 0.7$, E_i ($i = 1, \ldots ,4$) are the activation energies, A_i ($i = 1,\ldots,4$) are the pre-exponential factors, $\xi_i = normsinv(P_i)$ ($i = 1$ and 4) is a distribution parameter represented by the inverse of the normal distribution of the progress of reaction steps 1 and 4

$$P_1 = \frac{M_{wH_2O_a}\left[H_2O_a\right]}{\omega_{H_2O_a}\ \rho_{b,0}} \qquad P_4 = \frac{M_{wTATB}\left[TATB\right]}{(1 - \omega_{H_2O_a})\ \rho_{b,0}} \tag{11}$$

where $\omega_{H_2O_a}$ is the mass fraction of adsorbed water, $\rho_{b,0}$ is the initial bulk density of PBX 9502, $M_{wH_2O_a}$ and M_{wTATB} are the molecular weights of water and TATB. The parameters σ_i ($i = 1$ and 4) are the standard deviations of the activation energies E_i ($i = 1$ and 4), R is the universal gas

constant, and $(P/P_0)^{0.7}$ is pressure dependent ratio introduced to make the direct decomposition of TATB pressure dependent. The parameter P_0 is the initial pressure, and P is the average pressure in the PBX 9502 calculated using the equation

$$P = \frac{z\,n\,R\,T_{ave}}{V_g} \tag{12}$$

where z is the compressibility factor calculated using the BKW equation of state [4], n is the total number of moles of gases produced by the reactions, T_{ave} is an integral average of the temperature in the PBX 9502, and V_g is the volume occupied by the decomposition gases.

$$z = 1 + \frac{n\kappa\sum n_i k_i}{V_g(T_{ave}+\Theta)^\alpha} \exp\left(\beta\frac{n\kappa\sum n_i k_i}{V_g(T_{ave}+\Theta)^\alpha}\right) \tag{13}$$

where κ, n_i, k_i, Θ, and α are BKW parameters.

$$n = \int_V \left([H_2O_g]+[H_2O_m]+[Gas_m]+[Gas_t]\right)dV \tag{14}$$

$$T_{ave} = \frac{\int_V T\,dV}{\int_V dV} \tag{15}$$

$$V_g = \int_V \phi\,dV \tag{16}$$

where ϕ is the gas volume fraction defined by

$$\phi = 1 - \frac{S_f\,\rho_{c,0}(1-\phi_0)}{\rho_c} \tag{17}$$

where ρ_c, $\rho_{c,0}$, ϕ_0, and S_f are the condensed density, initial condensed density, initial gas volume fraction and reacted solid fraction respectively.

$$S_f = \frac{M_{wH_2O_a}[H_2O_a]+M_{wTATB}[TATB]+M_{wMF}[MF]+M_{wC}[Carbon_m]+M_{wC}[Carbon_t]}{\rho_{b,0}} \tag{18}$$

where M_{wMF} and M_{wC} are the molecular weights of mono-furazan and carbon respectively. The condensed density is defined as

$$\rho_c = \rho_{c,0}\left[1 - \beta_V(T-T_0)\right] \tag{19}$$

where T_0 is the initial temperature and β_V is the thermal expansion coefficient [5]

$$\beta_V = 99\times10^{-6} + 0.74\times10^{-6}\,T \tag{20}$$

The values of the parameters appearing in Eqs. (7)–(20) are given in reference [3]. The system of partial differential equations (PDEs) that involve the chemistry and conductive energy equations solved by Aria [1] in the PBX 9502 sphere are

10

$$\frac{\partial[H_2O_a]}{\partial t} = -r_1 \tag{21}$$

$$\frac{\partial[H_2O_g]}{\partial t} = r_1 \tag{22}$$

$$\frac{\partial[TATB]}{\partial t} = -r_2 - r_4 \tag{23}$$

$$\frac{\partial[MF]}{\partial t} = r_2 - r_3 \tag{24}$$

$$\frac{\partial[H_2O_m]}{\partial t} = r_2 \tag{25}$$

$$\frac{\partial[Gas_m]}{\partial t} = 6.52\, r_3 \tag{26}$$

$$\frac{\partial[Carbon_m]}{\partial t} = 4.18\, r_3 \tag{27}$$

$$\frac{\partial[Gas_t]}{\partial t} = 7.5\, r_4 \tag{28}$$

$$\frac{\partial[Carbon_t]}{\partial t} = 3.90\, r_4 \tag{29}$$

$$\rho_b\, C_b\, \frac{\partial T}{\partial t} = \nabla \bullet (k\, \nabla T) + \sum_{i=1}^{4} r_i\, h_{r_i}\, M_{w,i} \tag{30}$$

where ρ_b and C_b are the bulk density and heat capacity [6] respectively, k is the thermal conductivity as a function of temperature [7] , h_{r_i} ($i = 1,…,4$) is the reaction enthalpy for reaction steps 1–4 [3], and $M_{w,i}$ ($i = 1,…,4$) are the molecular weights for H_2O_a, $TATB$, MF, and $TATB$ respectively. The FE code Aria uses an operator splitting technique [8] to solve the system of PDEs represented by Eqs. (21)–(30). This technique considers that Eqs. (21)–(29) are defined locally as ordinary differential equations (ODEs) at the finite elements integration points. The species concentrations are viewed as state variables and this system of ODEs is integrated on an element-by-element basis at each FE time step, Δt_{FE}. A chemistry time step, $\Delta t_{chem.}$, is selected to integrate the system of ODEs represented by the mass conservation equations, (21)–(29), at the finite elements integration (Gauss) points. Aria contains a stiff ODE solver [9] that was used to integrate Eqs. (21)–(29).

Since this is as highly confined case with no expansion volume, the cook-off of the PBX 9502 up to thermal ignition (before confinement failure) is modeled assuming that its volume remains unchanged. Under this assumption, two limiting cases are considered (1) a case with pressure dependency which implies that no cracks develop and the gases stay inside closed pores and (2) a case without pressure dependency where cracks form and allow the gases to escape. For the case with no pressure dependency, the pressure ratio in Eq. (10) is replaced by $(P/P_0)^0$. The LT-55-1 experiment was simulated first considering these two limiting cases. Figure 11 shows thermocouples locations at the PBX mid-plane and Fig. 12 shows comparisons of cases (1) and (2) with thermocouples 31 and 44 which are located at the mid-plane center.
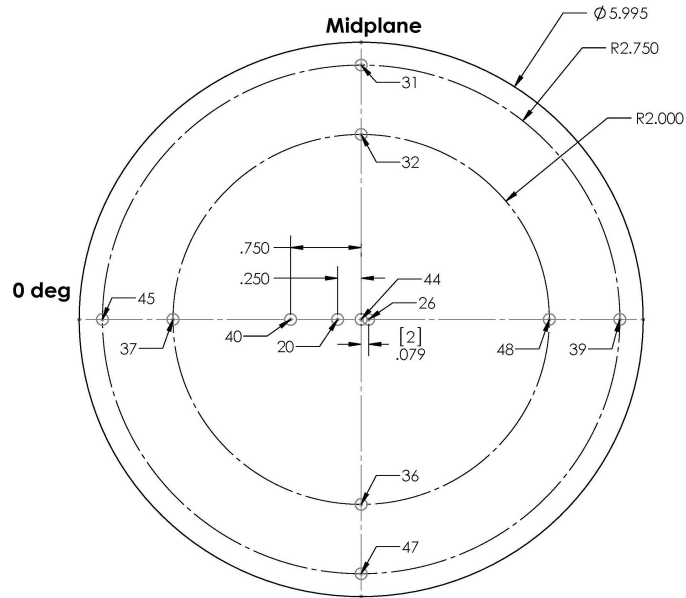
Figure 11. Thermocouples taped to the mid-plane of the bottom PBX hemisphere for the LT-55-1 test. Units are in inches.
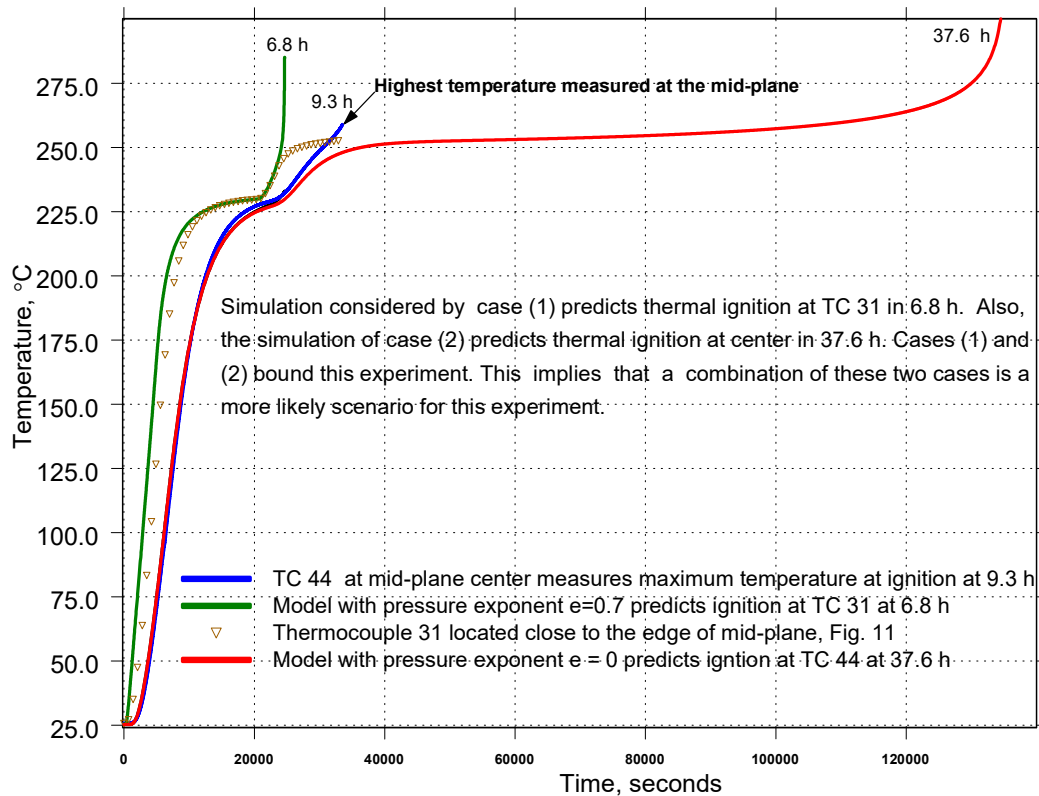

Figure 12. Comparison of simulations with experiments of two limiting cases for the the LT-55-1 experiment. Case (1) assumes that no cracks form and gases stay inside the pores and case (2) assumes that cracks form and gases can escape the PBX.

Figure 12 shows the results for cases (1) and (2). Since these two cases bound the experiment in terms of time to thermal ignition, a combination of these two cases is a more likely scenario for this experiment. The fact that the ignition time prediction of case (1) is closer to the experimental might imply that some damage and cracks form close to the outer surface of the PBX while a region close to the center of the PBX is still experiencing closed pore decomposition where the nucleation pores have not collapsed and contain thermal decomposition gases at high pressure. This situation produces a weaker pressure dependency of the global mechanism that defines the PBX decomposition process. Reference [3] introduced this pressure dependency in the direct decomposition of TATB, reaction 4, defined by the pressure ratio appearing in Eq. (10). This means that it is possible to estimate the value of the exponent e in Eq. (10) that will produce a close agreement between the PBX decomposition model predictions of time and location of ignition and this experiment. One parameter estimation simulations were carried out to calculate the value of the exponent e that produced a reasonable agreement between the cook-off model predictions and this experiment. The Aria FE model that uses the thermocouples located at the PBX 9502–steel interface (Figs. A1 and A2 of Appendix A) as boundary conditions was implemented for this estimation. The simulations were carried out using 64 processors in the Los Alamos National Laboratory (LANL) Moonlight super-computer. The estimated value of e is 0.47925. Figure 13 compares the calibrated FE response with the measurements of the thermocouples shown in Fig. 11.
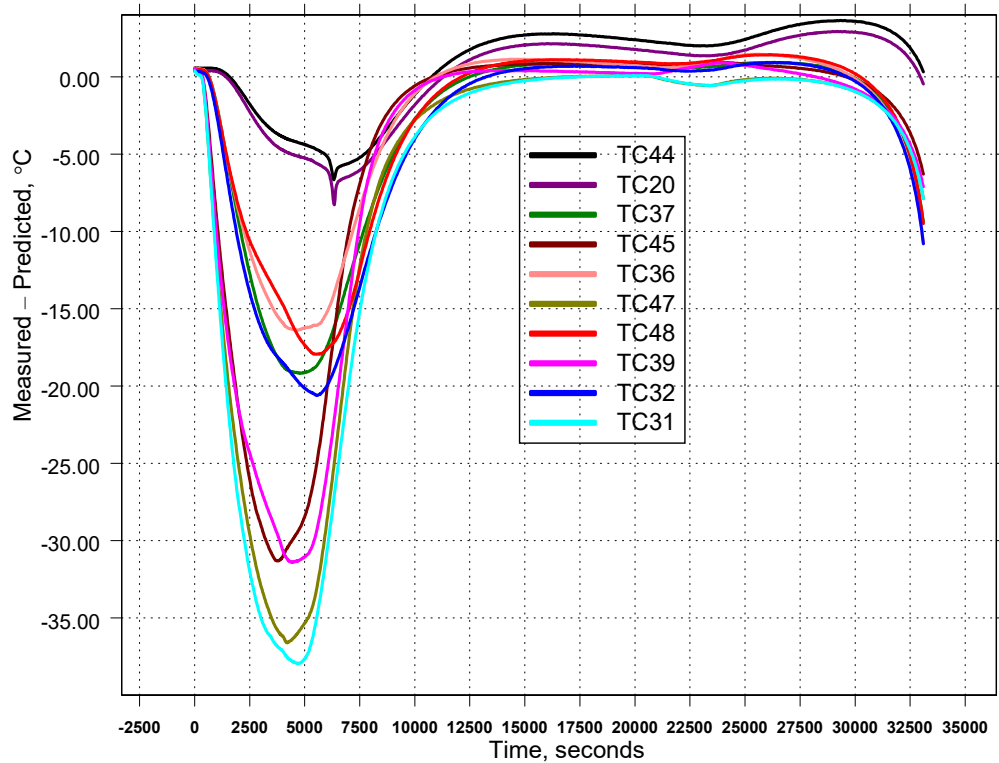

Figure 13. Comparison of the measurements of the thermocouples located at the mid–plane (see Fig. 11) with the FE model that uses $e = 0.47925$ as the exponent of the pressure ratio shown by Eq. (10). The error is defined as: Measured – Predicted temperatures.

13

The time to thermal ignition for this experiment is 33523 s (9.3 h) and the calibrated model predicts ignition at 33789 s with a -0.8 % difference. Figure 13 shows that the error in the predicted temperature is large for $0 \leq t \leq 10500$ s. The predictions at the TC45, TC31, TC 39, and TC47 thermocouple locations have the largest errors. The magnitudes of these errors are greater than 30 °C for 2285 s $\leq t \leq 6066$ s. Note that these thermocouple locations are the ones that are closer to the outer surface of the PBX at the mid-plane (see Fig. 11). The main reason for these errors is the thermal resistance produced by a layer of air between the 4340 steel bowl and the outer surface of the bottom PBX hemisphere. This air layer has an average thickness of 2 mm at the beginning of the experiment. As the PBX expands during the first heating ramp, the thickness of this air gap decreases until its effect becomes negligible for times greater than 10500 s. As mentioned previously, the thermocouples located at the PBX 9502 hemisphere–steel bottom interface were taped to the metal spherical cavity. Figure 14 shows these thermocouples taped to the steel bowl. Since these thermocouples were also used to define a temperature boundary conditions on the outer surface of the PBX 9502 sphere, the FE model predicts higher temperatures for $0 \leq t \leq 13000$ s at the thermocouple locations TC 45, TC 37, TC 31, TC 32, TC 39, TC 48, TC 47, and TC 36 shown in Fig. 11. Figure 15 shows the air gap between the steel bowl and the PBX hemisphere when they were in the process of being assembled. Also, Fig. 15 shows a thermocouple taped to the equator on the metal side of the interface.
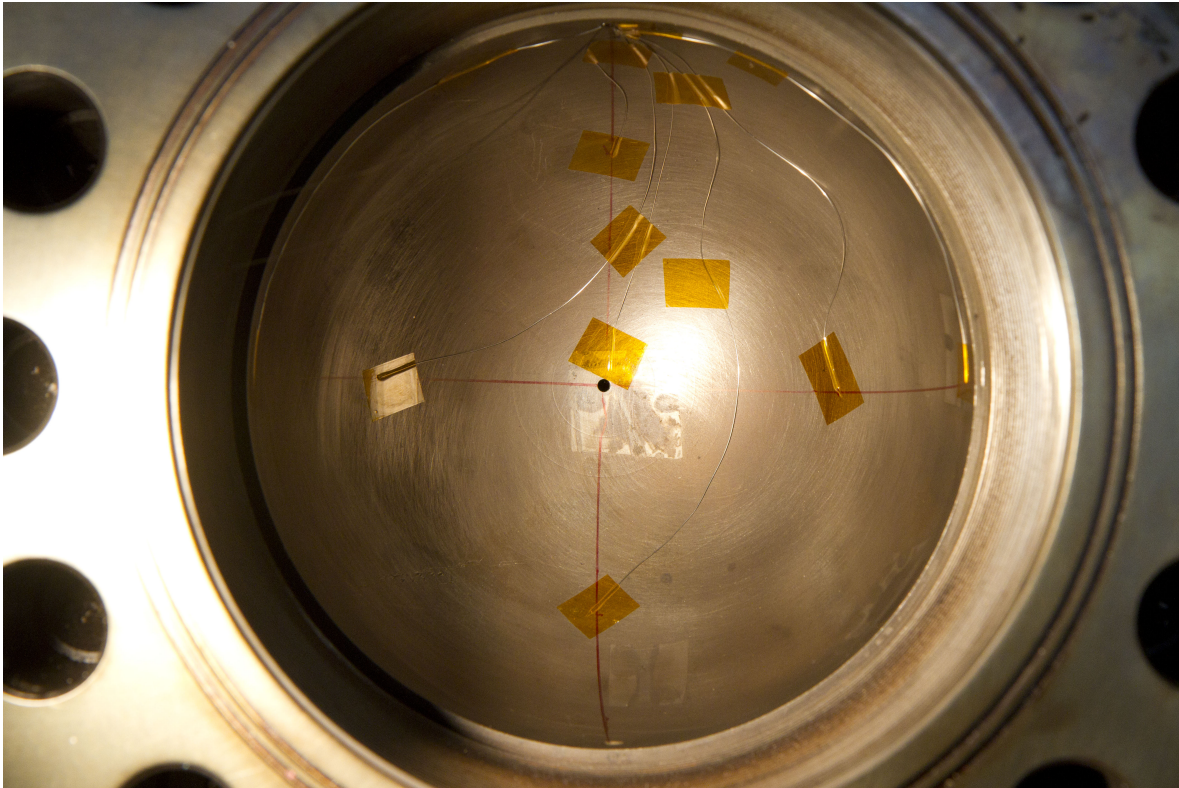

Figure 14. Thermocouples taped to the steel bowl for the LT-55-1 experiment. These thermocouples were used to define the temperature boundary condition on the outer surface of the bottom PBX hemisphere.
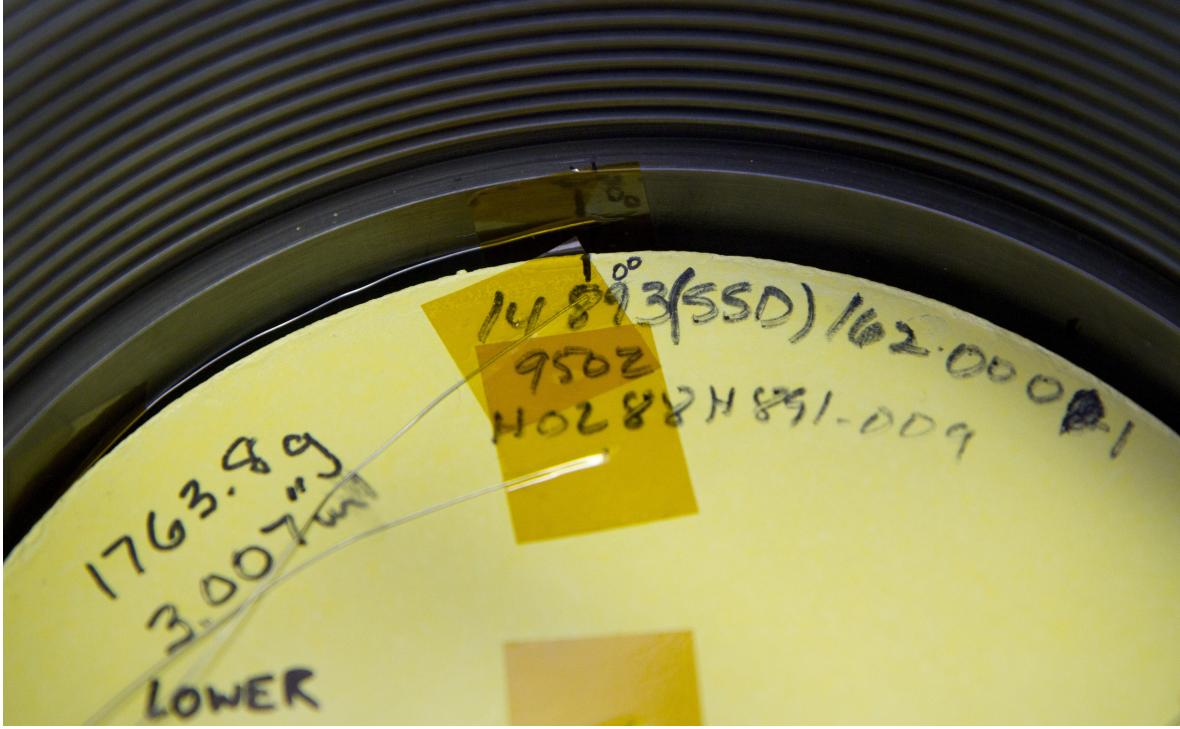
Figure 15. Bottom PBX 9502 hemisphere placed on top of the steel bowl. The photo shows the thermocouple taped at the equator on the steel bowl and the 2 mm air gap between the PBX hemisphere and the metal.

The temperature measurements at the thermocouple locations TC 45, TC 37, TC 31, TC 32, TC 39, TC 48, TC 47, and TC 46 shown in Fig. 11 can be used to calculate the temperatures on the outer surface of the PBX on the edge of the mid-plane at 0, 90, 180, and 270 degrees. This calculation can produce the actual temperatures at these locations and should provide a more realistic boundary condition that takes into account the effects of the air gap which are significant in the time interval $0 \leq t \leq 13000$ s. An estimate of the energy flowing by conduction at the locations TC45, TC31, TC39, and TC47 as a function of time can be used to obtain a first guess for the surface temperatures on the edge of the mid-plane at 0, 90, 180, and 270 degrees. For example, assuming a one-dimensional spherical layer located between TC 45 and TC 37, the energy flowing into location 45 can be approximated as

$$q\big|_{45} = \frac{4 \pi k \left(T_{37} - T_{45}\right)}{(1/R_1) - (1/R_2)} \tag{31}$$

where T_{37} and T_{45} are the thermocouple measurements at TC 37 and TC 45, k is the thermal conductivity of PBX 9502 [7] evaluated at $(T_{37} + T_{45})/2$, $R_1 = 2$ in, and $R_2 = 2.75$ in. The radial locations R_1 and R_2 are shown in Fig. 11. Next, it is assumed that the energy flowing into location 45 is the same as the energy flowing into location 1 shown in Fig. 16. Note that this assumption is reasonable because the distance between locations 1 and 45 is only 6 mm. Figure 16 also shows additional locations where the energy flowing into the PBX is estimated using equations of the same type of Eq. (31). The heat at locations 31, 39, and 47 is given by Eqs. (32),
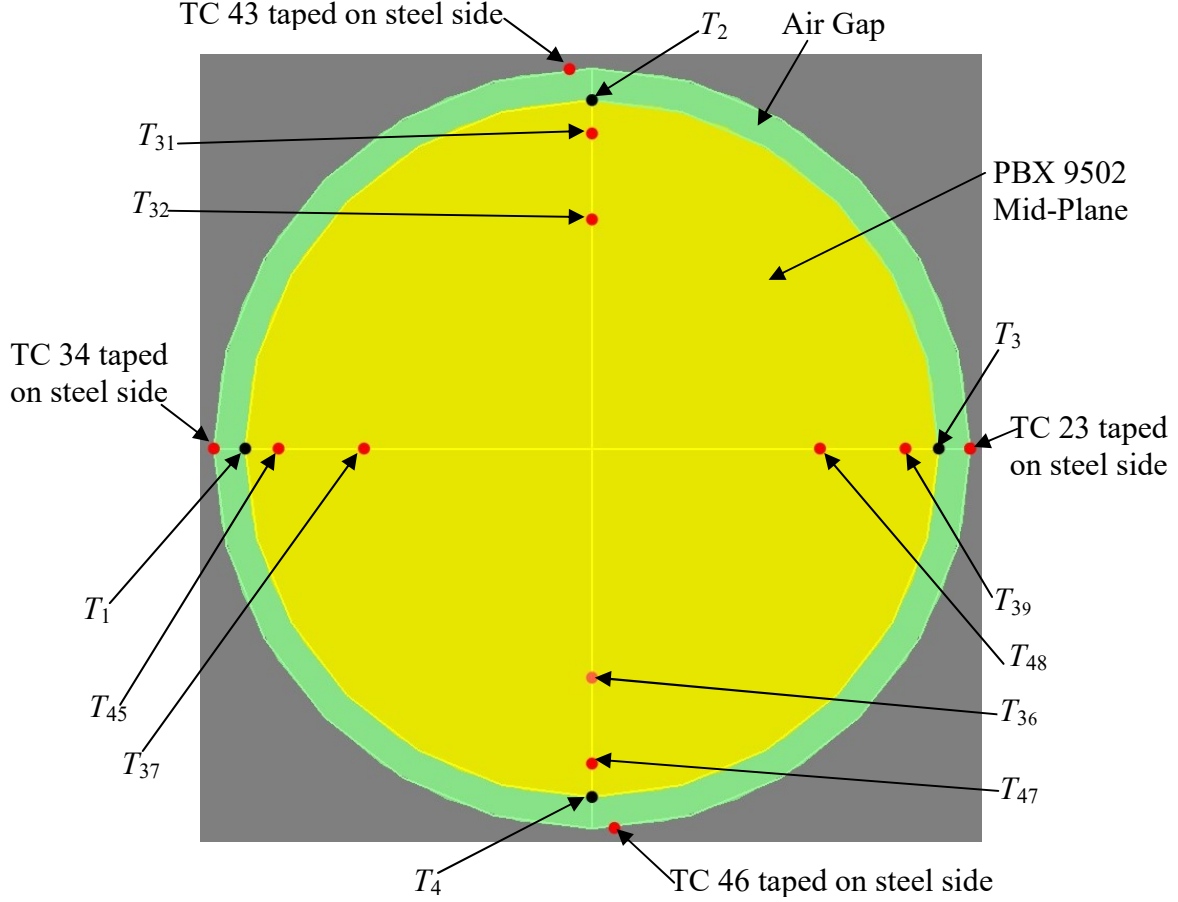
Figure 16. Red dots represent thermocouple locations and block dots represent the locations where surface temperatures were calculated.

$$q|_{31} = \frac{4\pi k \left(T_{32} - T_{31}\right)}{(1/R_1) - (1/R_2)} \tag{32}$$

$$q|_{39} = \frac{4\pi k \left(T_{48} - T_{39}\right)}{(1/R_1) - (1/R_2)} \tag{33}$$

$$q|_{47} = \frac{4\pi k \left(T_{36} - T_{47}\right)}{(1/R_1) - (1/R_2)} \tag{34}$$

(33), and (34). A first approximation to the surface temperatures T_1, T_2, T_3, and T_4 can be obtained assuming that $q|_{45} \approx q|_1$, $q|_{31} \approx q|_2$, $q|_{39} \approx q|_3$, and $q|_{47} \approx q|_4$. Under these assumptions, approximate expressions for the surface temperatures T_1, T_2, T_3, and T_4 are obtained as

$$T_1^1 = T_{45} - \frac{q|_1 (R_0 - R_2)}{4 \pi k R_0 R_2} \quad \text{for } 0 \leq t \leq 13000 \text{ s} \tag{35}$$

$$T_2^1 = T_{31} - \frac{q|_2 (R_0 - R_2)}{4 \pi k R_0 R_2} \quad \text{for } 0 \leq t \leq 13000 \text{ s} \tag{36}$$

$$T_3^1 = T_{39} - \frac{q|_3 (R_0 - R_2)}{4 \pi k R_0 R_2} \quad \text{for } 0 \leq t \leq 13000 \text{ s} \tag{37}$$

$$T_4^1 = T_{39} - \frac{q|_4 (R_0 - R_2)}{4 \pi k R_0 R_2} \quad \text{for } 0 \leq t \leq 13000 \text{ s} \tag{38}$$

where R_0 is the outer radius of the PBX (3 in), the superscript 1 in Eqs. (35)–(38) is used to imply that they represent the first guess for the surface temperatures. A computational scheme was developed and implemented to calculate these surface temperatures. The first iteration step in this scheme is to replace the temperatures given by thermocouples TC 34, TC 43, TC 23, and TC 46 (see Fig. 16) in the interval $0 \leq t \leq 13000$ s by the first estimate of the surface temperatures given by Eq. (35)–(38) and run the FE model with these surface temperatures as boundary conditions. This first iteration produces the FE model predicted temperatures T_{fe45}^1, T_{fe31}^1, T_{fe39}^1, and T_{fe47}^1 at thermocouple locations 45, 31, 39, and 47 respectively. The second iteration consists of a correction to the surface temperatures calculated with Eqs. (35)–(38) as

$$T_1^2 = \frac{T_{45}}{T_{\text{fe45}}^1} T_1^1 \quad \text{for } 0 \leq t \leq 13000 \text{ s} \tag{39}$$

$$T_2^2 = \frac{T_{31}}{T_{\text{fe31}}^1} T_2^1 \quad \text{for } 0 \leq t \leq 13000 \text{ s} \tag{40}$$

$$T_3^2 = \frac{T_{39}}{T_{\text{fe39}}^1} T_3^1 \quad \text{for } 0 \leq t \leq 13000 \text{ s} \tag{41}$$

$$T_4^2 = \frac{T_{47}}{T_{\text{fe47}}^1} T_4^1 \quad \text{for } 0 \leq t \leq 13000 \text{ s} \tag{42}$$

where T_{45}, T_{31}, T_{39}, and T_{47} are the thermocouple measurements at locations 45, 31, 39 and 47 respectively. The surface temperatures T_1^1, T_2^1, T_3^1, and T_4^1 used in the previous iteration are replaced with the corrected surface temperatures T_1^2, T_2^2, T_3^2, and T_4^2 and the FE model is run again using these surface temperatures as boundary conditions. This second iteration predicts temperatures that are in good agreement with thermocouples 45, 37, 31, 32, 39, 48, and 47. For this reason, no additional iterations are carried out. Figure 17 shows the errors associated with the FE predictions at these thermocouple locations. It is pointed out that the iterations carried out using this function estimation scheme were done running the FE model from zero to a final time of 13000 s. Also, there is a mild endothermic effect in this time interval caused by the release of
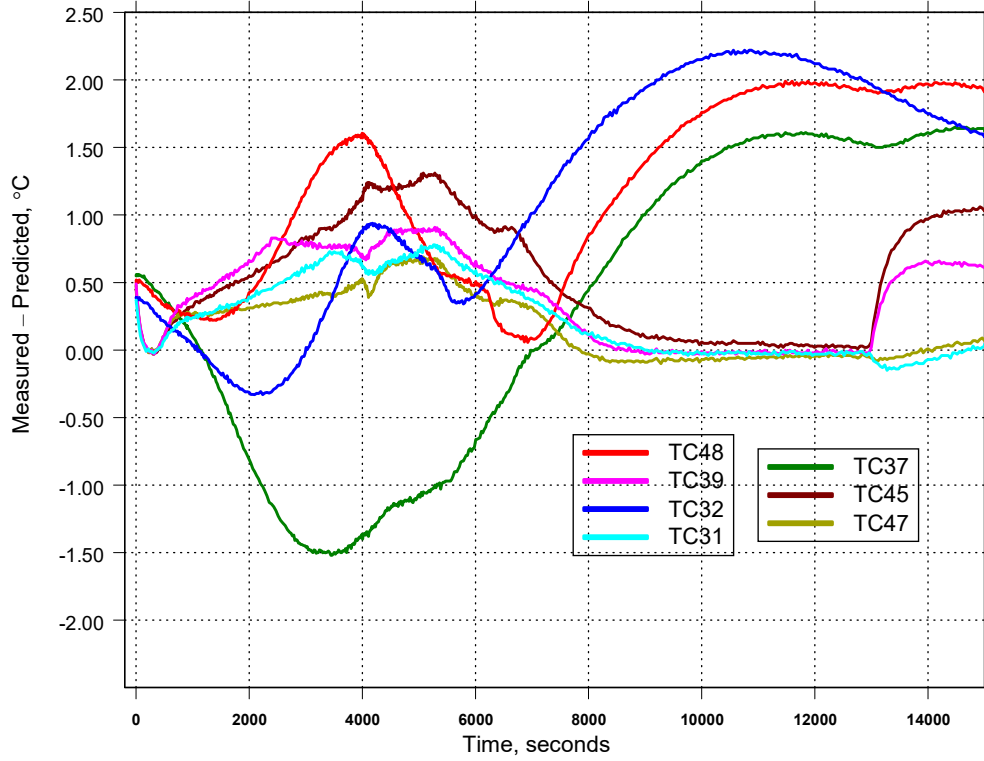
Figure 17. Errors associated with the estimation of functions $T_1^2(t)$, $T_2^2(t)$, $T_3^2(t)$, and $T_4^2(t)$ defined by Eqs. (39)–(42).

adsorbed water in the first reaction step of the mechanism which doesn't have a significant influence on the estimation of these surface temperatures. Note from Fig. 17 that the errors shown in Fig. 13 in the interval $0 \leq t \leq 13000$ s were decreased significantly by the estimation of the functions defined by Eqs. (39)–(42). The thermocouples used for these experiments were of type K. These thermocouples were constructed from special limits of error wire that provides a measurement accuracy of ± 1.1 °C. The errors in Fig. 17 fluctuate between -1.5 °C and $+2.25$ °C. The FE predictions at locations 32, 37, and 48 experienced the largest errors. However, the differences between these errors and the magnitude of the measurement accuracy of 1.1 °C are not larger than 1.15 °C. Additional simulations were carried out using the surface temperatures defined by Eqs. (39)–(42) and the PBX 9502–steel interface thermocouples shown in Figs. A1 and A2 with the exception of thermocouples 34, 43, 23, and 46 for $t \leq 13000$ s. This was done to estimate the value of the pressure exponent e and determine if the presence of the air gap has a significant influence on the pressure exponent. The estimated value of e is 0.49 which is close to the previously estimated value of 0.47925. The predicted time to thermal ignition is 33261 s which differs $+0.8$ % from the experimental. Figure 18 shows the FE model prediction errors at the thermocouple locations shown in Fig. 11 in the interval $0 \leq t \leq 31500$ s. Figure 18 shows that the model has the largest errors at TC 20, TC 36, and TC 44 for $7100 \leq t \leq 17503$ s. These errors begin to fall within the type-K thermocouple errors for $17503 \leq t \leq 31500$. So, when the second heating ramp on the outer surface of the steel vessel is started (20380 s), the FE model prediction errors at the mid-plane are already between -1 °C and $+3$ °C. Also, Fig. 19 shows the FE model prediction errors at the
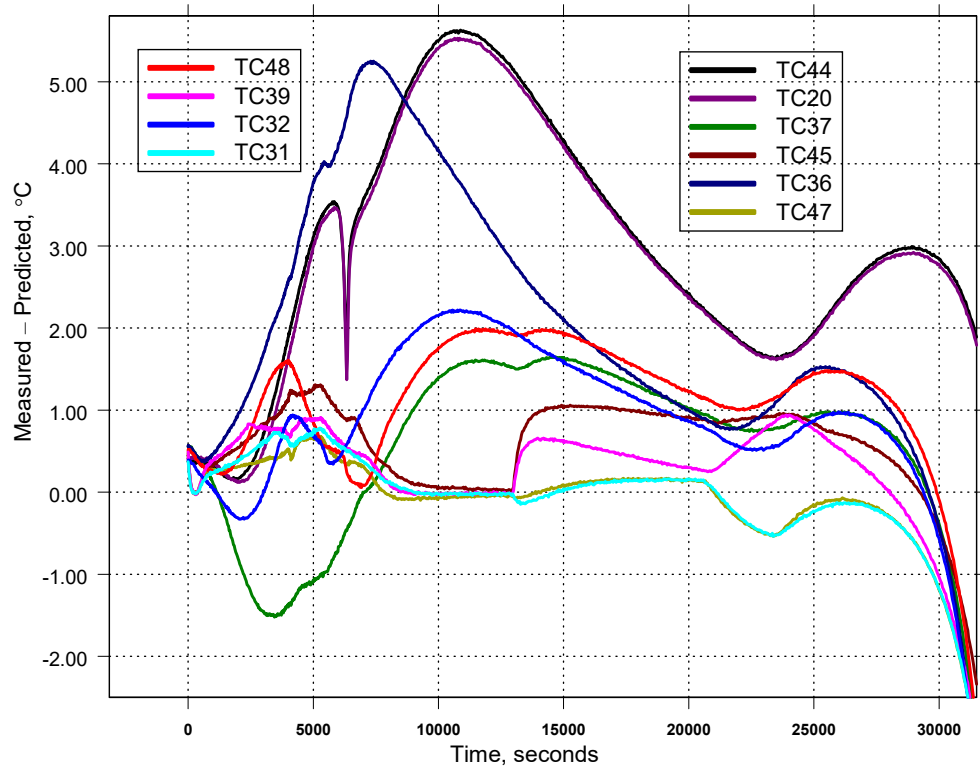
18

Figure 18. Finite element model prediction errors at the thermocouple locations shown in Fig. 11 using a pressure ratio exponent of 0.49 in Eq. (10).
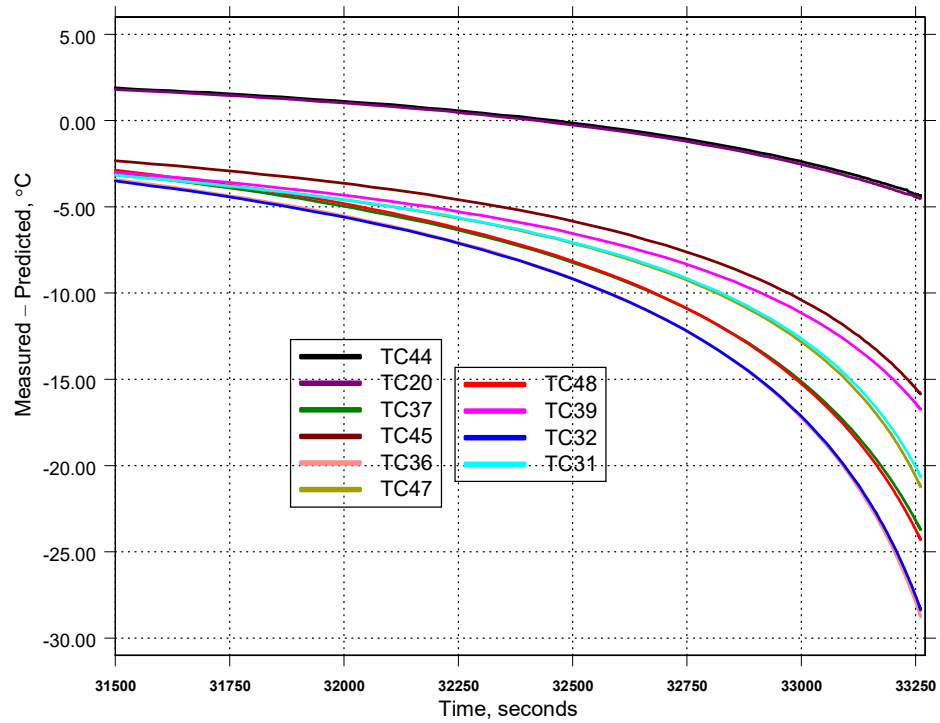

Figure 19. Finite element model prediction errors at the thermocouple locations shown in Fig. 11 using a pressure ratio exponent of 0.49 in Eq. (10).
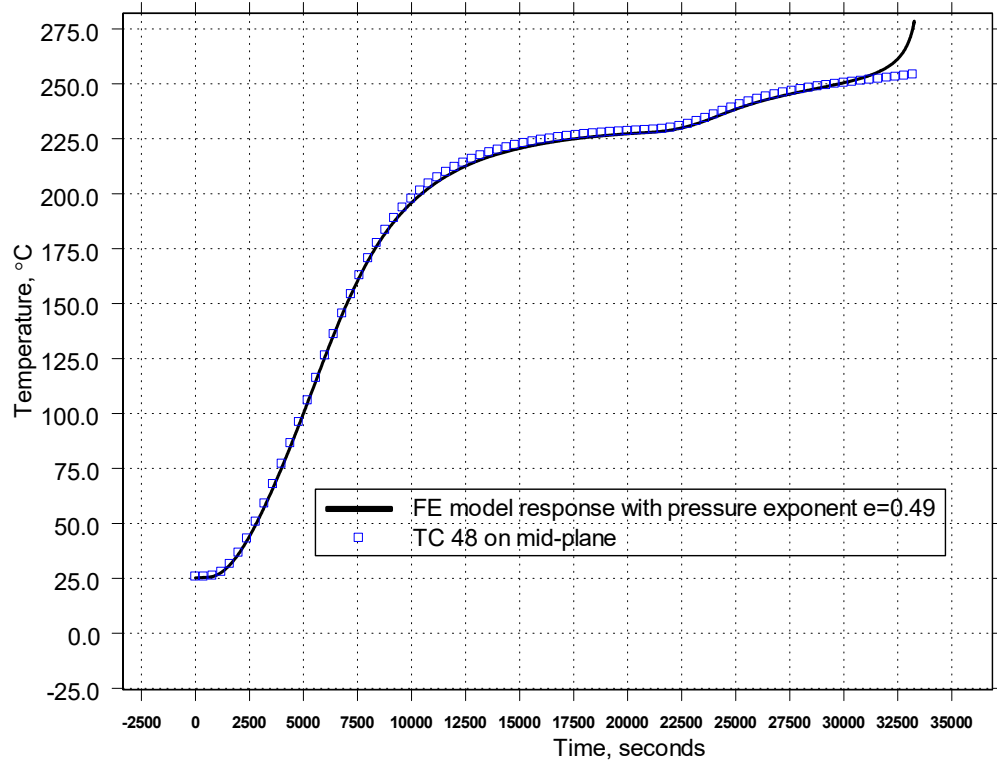
19

Figure 20. Comparison of measured and predicted temperatures at TC 36. Finite element model uses surface temperatures that include Eqs. (39)–(42).
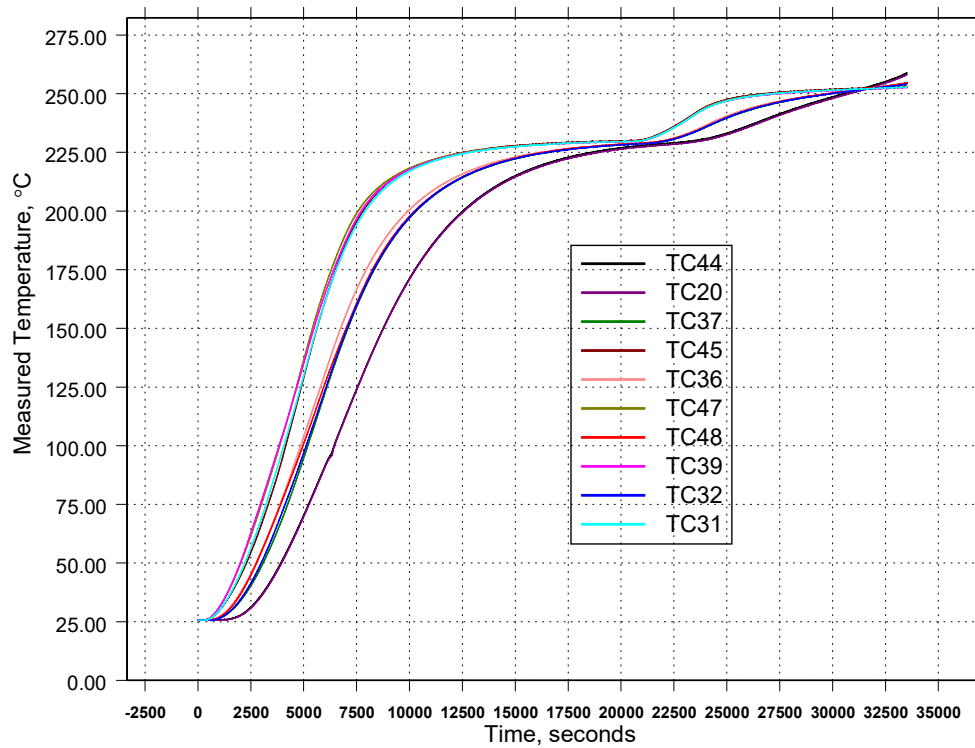

Figure 21. Temperatures measured at the mid-plane for the LT-55-1 experiment.

thermocouple locations shown in Fig. 11 for $31500 \leq t \leq 33261$ s. Figure 19 shows that the magnitude of the error begins to increase at 31750 seconds and has its largest value at the end of the simulation. The PBX chemistry model begins to predict an exponential thermal runaway at thermocouple locations 45, 37, 31, 32, 39, 48, 47, and 36 for $t > 31500$ s. This exponential increase in temperature causes the increase in error seen in Fig. 19 for these predictions. For example, Fig. 20 compares the temperatures predicted by the model with thermocouple 48 and shows the predicted exponential increase in temperature close to ignition time. The volumetric source term defined by the PBX chemistry model in Eq. (30) causes this exponential increase. The error seen in Fig. 19 might be due to the thermal resistance present at the mid–plane between the two PBX hemispheres. The FE model of the PBX hemispheres doesn't take into consideration this thermal resistance. It is pointed out that the thermocouples installed at the mid–plane didn't measure an extended exponential thermal runaway like the one shown in Fig. 20. This is an indication that ignition happened somewhere above or below the mid-plane. Figure 21 shows the mid-plane thermocouples measurements. The temperature distribution obtained from the FE simulation revealed that thermal ignition occurred inside the top PBX hemisphere. Figure 22 shows one quarter of the top PBX hemisphere where thermal ignition took place. The point with the maximum temperature inside the hot spot shown in Fig. 22 is located 1.9 in above the mid–plane and 1.4 in to the left of the vertical spherical axis. The confidence in the predicted
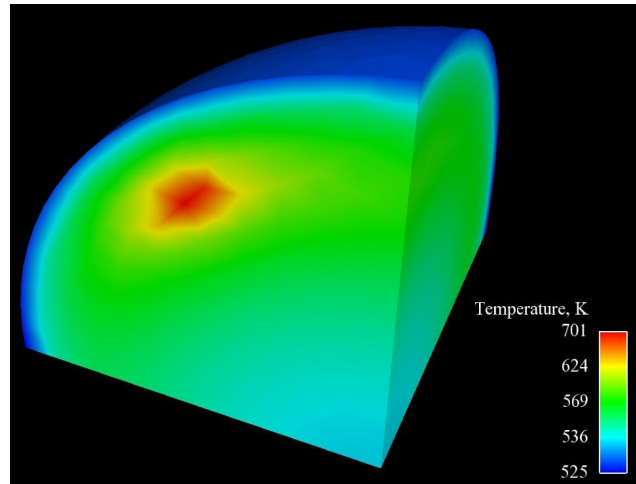

Figure 22. Temperature distribution in a quarter of the top hemisphere.

location of ignition shown in Fig. 22 is reinforced by the agreement between the FE model with the thermocouple measurements in the mid-plane. The prediction errors seen in Figs. 17 and 18 are close to the measurement errors with the exception of TC 20, 36, and 44 in the interval $7100 \leq t \leq 17503$ s. Note that the prediction at the center experiences the largest error of +5.8 °C in this time interval and this error decreases for times greater than 12000 s until it falls between the range of –1 °C and +3 °C for times greater than 17503 s. The PBX chemistry model with pressure ratio exponent $e = 0.47925$ was also used to simulate this experiment using the surface temperatures estimated by Eqs. (39)–(42). Table 1 summarizes the simulations carried out with the calibrated models and shows that the presence of the 2 mm air gap between the metal and the bottom PBX hemisphere doesn't have a significant influence on the predicted times of thermal ignition. Also, the predicted locations of ignition for the cases shown in Table 1 are practically the same.

Table 1. Summary of the calibrated model simulations, boundary conditions, and predictions. Boundary conditions used for $t > 13000$ s were taken from thermocouple measurements at locations shown in Figs. A1 and A2. The error is defined as (Measured – Predicted)/Measured ×100.

Pressure ratio exponent e used in Eq. (10).	Boundary temperatures at the equator used in $0 \leq t \leq 13000$ s.	Thermal ignition time percentage error, %
0.49	Eqs. (39)–(42)	+0.8
0.47925	TC 34, 43, 23, and 46.	−0.8
0.47925	Eqs. (39)–(42)	−1.0

Finite element simulations of test LT-55-2

The second heavily confined test was simulated applying the same approach used to simulate the first test. The thermocouple measurements at the PBX 9502–steel interface were used to define a temperature boundary condition on the outer surface of the PBX sphere. The locations of these thermocouples are shown in Figs. A3 and A4 of Appendix A. The FE response was compared with ten thermocouple measurements at the mid-plane. Figure 23 shows the location of these mid-plane thermocouples. Also, Fig. 24 shows the thermocouples taped at the equator of the steel bowl spherical cavity. The assembly procedure for test 2 was the same as for test 1. There is also a 2 mm layer of air present between the 4340 steel confinement and the outer surface of the PBX sphere at the beginning of this experiment. As the PBX sphere expands during the first heating ramp, the thickness of this air gap decreases until its effect becomes negligible when the steel and PBX surfaces meet and begin to develop some contact pressure. Figure 25 depicts a top–down view of the mid–plane with a sketch that shows the steel, air gap,

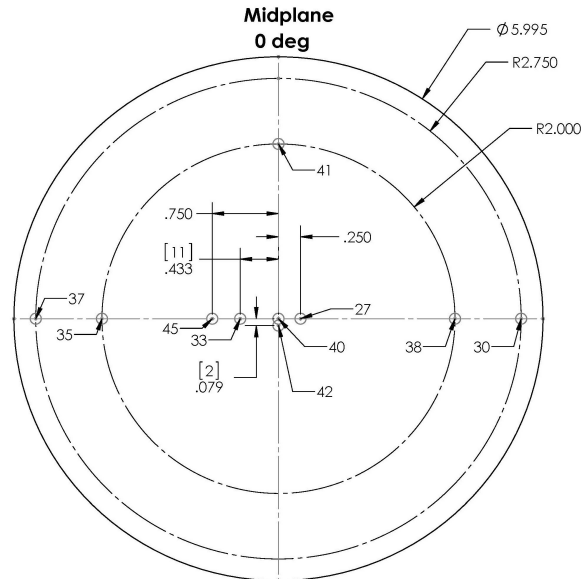Figure 23. Thermocouples taped to the mid-plane of the bottom PBX hemisphere for the LT-55-2 test. Units are in inches.
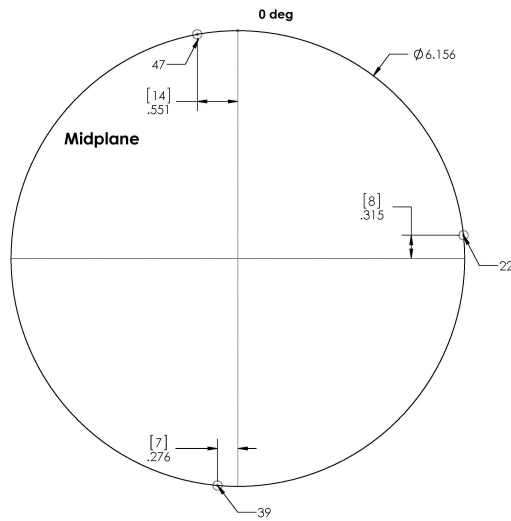
Figure 24. Thermocouples taped at the equator on the steel bowl spherical cavity for the LT-55-2 test. Units are in inches.
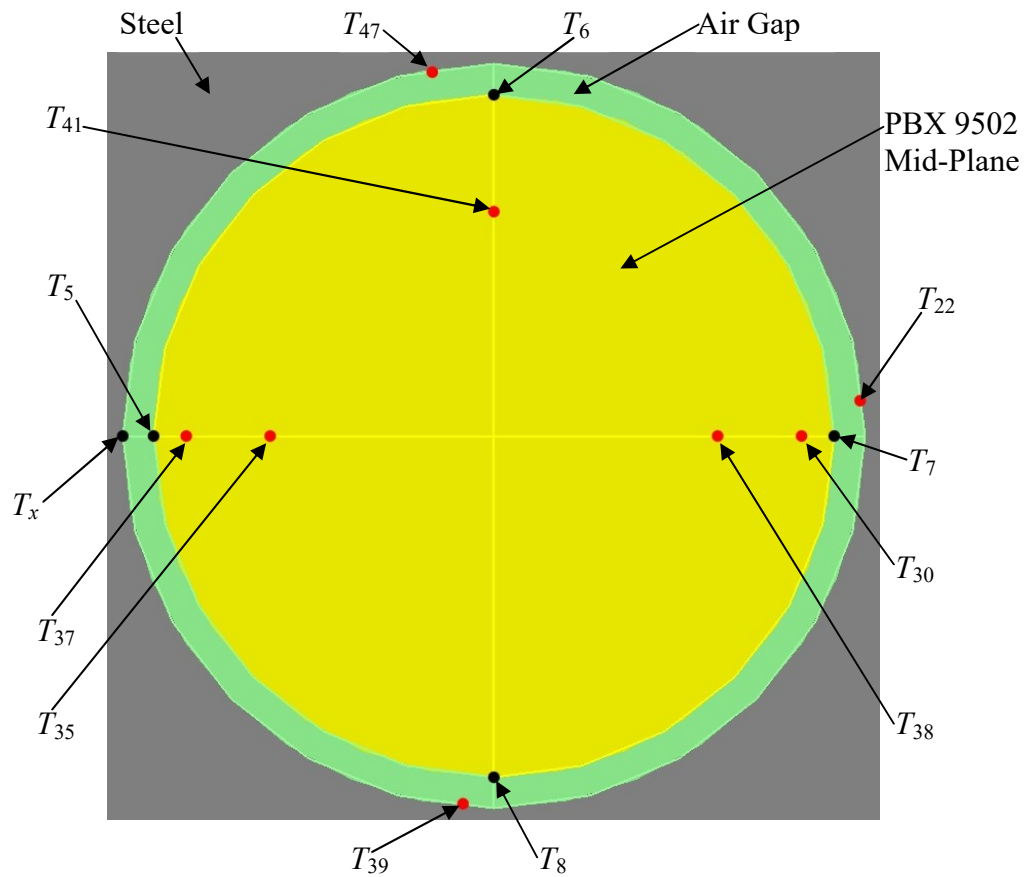

Figure 25. Red dots represent thermocouple locations and block dots represent the locations where surface temperatures were calculated. This is a top–down view.

PBX mid–plane, thermocouple numbers and locations, and the locations where surface temperatures were calculated. Note from Fig. 24 that there was no thermocouple installed at the equator on the 270° position for this experiment. The symbol T_x appearing in Fig. 25 represents the temperatures calculated to replace this missing thermocouple. The surface temperature T_x was calculated using the experimental information from thermocouples 22, 30, and 37. Note that thermocouples 30 and 27 are close to the outer surface of the PBX sphere. The distance along the horizontal axis (see Fig. 23) between the mid-plane thermocouple 30 and the outer surface of the PBX is only 6 mm. Also, the horizontal distance between thermocouple 37 and the outer surface of the PBX is 6 mm. Figures 26 and 27 compare the temperature measurements of thermocouples 30 and 37. Note from Fig. 26 that the two temperature curves have very similar shapes. Also, Fig. 27 shows that the difference between thermocouples 30 and 37 is small taking into consideration the thermocouples total error. The similarity between the thermocouple measurements at locations 30 and 37 implies that the thermal contact conductances (in W/m^2 K) at the interface locations x–5 and 22–7 shown in Fig. 25 are also similar. The energies in the form of heat coming into locations 5 and 7 shown in Fig. 25 can be expressed as

$$q_5 = h_{x-5} \left(T_x - T_5 \right) A \tag{43}$$
$$q_7 = h_{22-7} \left(T_{22} - T_7 \right) A \tag{44}$$

where A is the area, and h_{x-5} and h_{22-7} are the thermal conductances at the interface locations x–5 and 22–7 respectively. Dividing Eq. (43) by $A \, T_{37} \, h_{x-5}$ and Eq. (44) by $A \, T_{30} \, h_{22-7}$ one gets
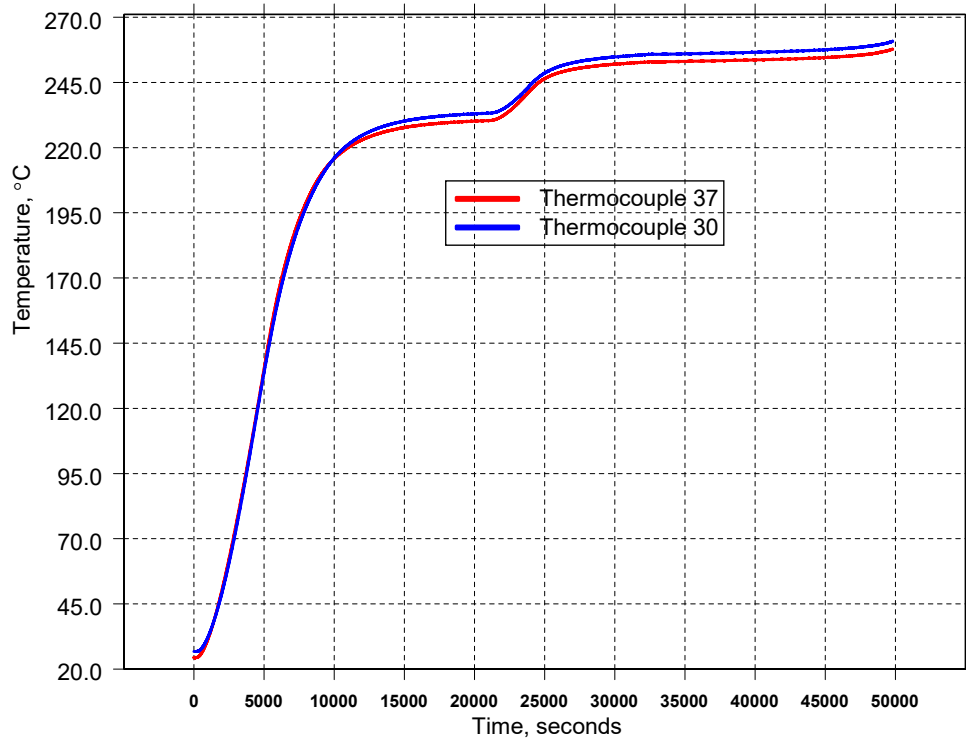

Figure 26. Comparison of mid-plane thermocouples 30 and 37. See Fig. 23.
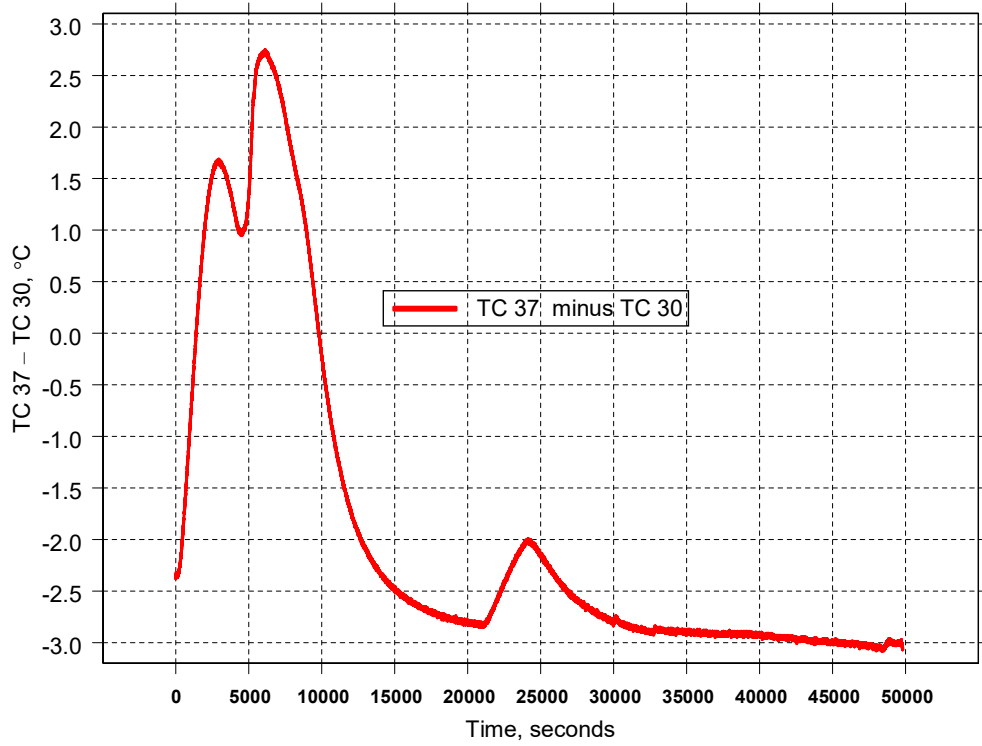
Figure 27. Comparison of mid-plane thermocouples 30 and 37. See Fig. 23.

$$\frac{q_5}{A\,h_{x-5}\,T_{37}} = \left(\frac{T_x}{T_{37}} - \frac{T_5}{T_{37}}\right) \tag{45}$$

$$\frac{q_7}{A\,h_{22-7}\,T_{30}} = \left(\frac{T_{22}}{T_{30}} - \frac{T_7}{T_{30}}\right) \tag{46}$$

Because of the similarities between the temperatures measured by thermocouples 30 and 37, it is reasonable to assume that

$$\frac{q_5}{A\,h_{x-5}\,T_{37}} \approx \frac{q_7}{A\,h_{22-7}\,T_{30}} \tag{47}$$

equations (45)–(47) lead to

$$\left(\frac{T_x}{T_{37}} - \frac{T_{22}}{T_{30}}\right) \approx \left(\frac{T_5}{T_{37}} - \frac{T_7}{T_{30}}\right) \tag{48}$$

The quantities q_5 and q_7 can also be approximated using finite differences as

$$q_5 = k\,A\,\frac{T_5 - T_{37}}{\Delta R} \tag{49}$$

$$q_7 = k\,A\,\frac{T_7 - T_{30}}{\Delta R} \tag{50}$$

25

where k is the thermal conductivity of PBX 9502 and ΔR is equal to 6 mm. Multiplying Eq. (49) by the ratio $\Delta R/(k\,A\,T_{37})$ and Eq. (50) by $\Delta R/(k\,A\,T_{30})$, and assuming that the resulting dimensionless quantities are approximately equal $\Delta R\,q_5/(k\,A\,T_{37}) \approx \Delta R\,q_7/(k\,A\,T_{30})$, one gets

$$\left(\frac{T_5}{T_{37}} - \frac{T_7}{T_{30}}\right) \approx 0 \tag{51}$$

Equations (48) and (51) allow obtaining an approximation for the temperature T_x as

$$T_x \approx \frac{T_{22}}{T_{30}}\,T_{37} \tag{52}$$

   The LT-55-2 test was designed to be a sealed test. However, the static pressure measurement data shown in Fig. 9 indicates that a gas leak developed during the experiment. For this reason, this experiment is modeled first considering two limiting cases: (1) a case with pressure dependency which implies that no cracks develop and the gases stay inside closed pores and (2) a case without pressure dependency where cracks form and allow the gases to escape. For the case with no pressure dependency, the pressure ratio in Eq. (10) is replaced by $(P/P_0)^0$. Figure 28 shows the results of the model for cases (1) and (2). Figure 28 shows that cases (1) and (2) bound
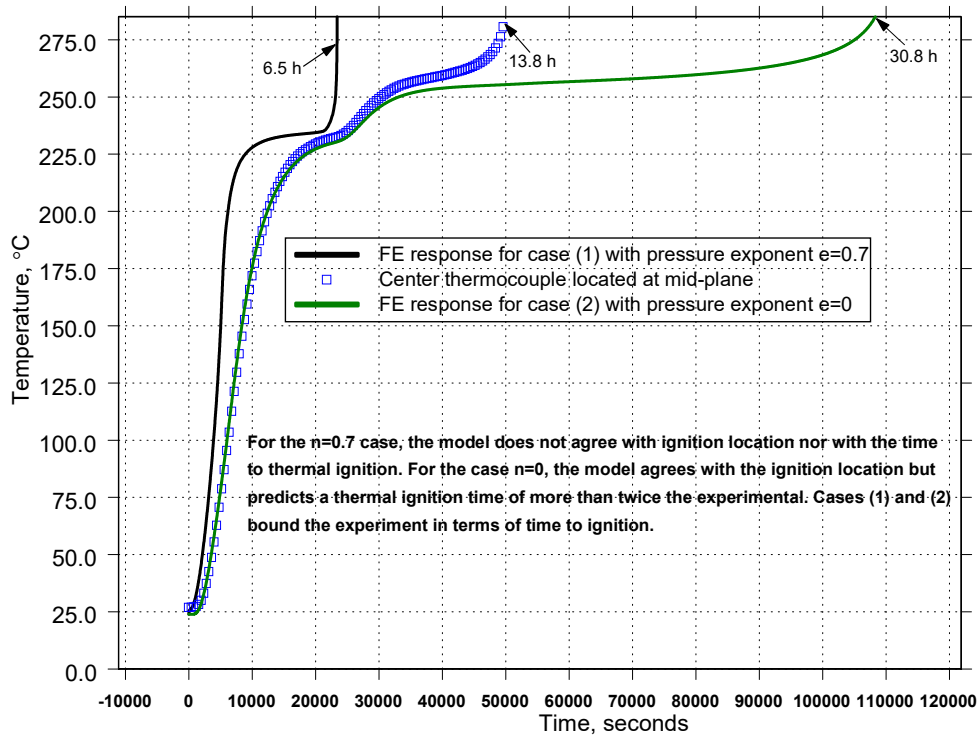
Figure 28. Comparison of simulations with experiments of two limiting cases for the the LT-55-2 experiment. Case (1) assumes that decomposition mechanism is pressure dependent and case (2) assumes no pressure dependency on the mechanism.

the experiment in terms of time to ignition. This outcome is similar to the results obtained for the LT-55-1 experiment. This is to be expected since both experiments experienced leakage of thermal decomposition gases. A more likely modeling scenario for this experiment is a combination of cases (1) and (2). For this reason, simulations were carried out to estimate a value of the exponent e in Eq. (10) that produced a reasonable agreement with the time and location of thermal ignition. An estimated value of e equal to 0.239 produced a good agreement with the experimental time and location of ignition. The experimental time to ignition for this experiment is 49803 s and the predicted time to thermal ignition using the exponent $e = 0.239$ is 50822 s. The percentage difference is only +2%. Figure 29 shows plots of the FE temperature predictions errors at the thermocouple locations on the mid-plane shown in Fig. 23. Figure 29 shows that the
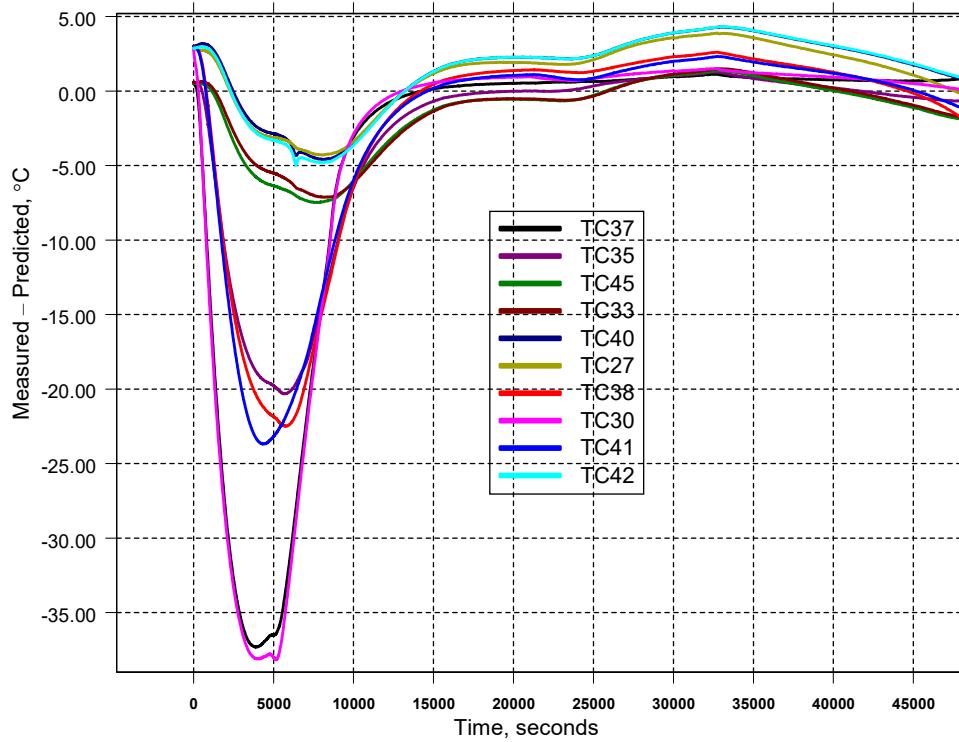

Figure 29. Comparison of the measurements of the thermocouples located at the mid–plane (see Fig. 23) with the FE model that uses $e = 0.23900$ as the exponent of the pressure ratio shown by Eq. (10). The error is defined as: Measured – Predicted temperatures.

error in the predicted temperature is large for $0 \leq t \leq 13000$ s. The FE predictions at the TC 30, TC 37, TC 33, TC 35 and TC 41 thermocouple locations have the largest errors. The magnitudes of the maximum errors are greater than 35 °C for TC 30 and TC 37. Note that these thermocouple locations are the ones that are closer to the outer surface of the PBX at the mid-plane (see Fig. 23). A comparison of Figs. 13 and 29 shows that the errors associated with the LT-55-1 and LT-55-2 experiments have similar behaviors in the interval $0 \leq t \leq 13000$ s. The FE temperature predictions at the thermocouple locations that are installed closer to the outer surface of the PBX at the mid-plane have the largest errors in the interval $0 \leq t \leq 13000$ s. This similarity is to be expected because the first heating ramps applied on the outer surface of the steel

27

confinement were similar for both experiments. Figure 30 compares the effects of these ramps on the temperatures measured by the thermocouples installed at the equator of the steel confinement spherical cavity for the LT-55-1 and LT-55-2 experiments. Figure 30 shows that these sensors measured a heating rate of 2 °C/min for both experiments. Also, this figure shows that the temperature soaks averaged around 230 °C.
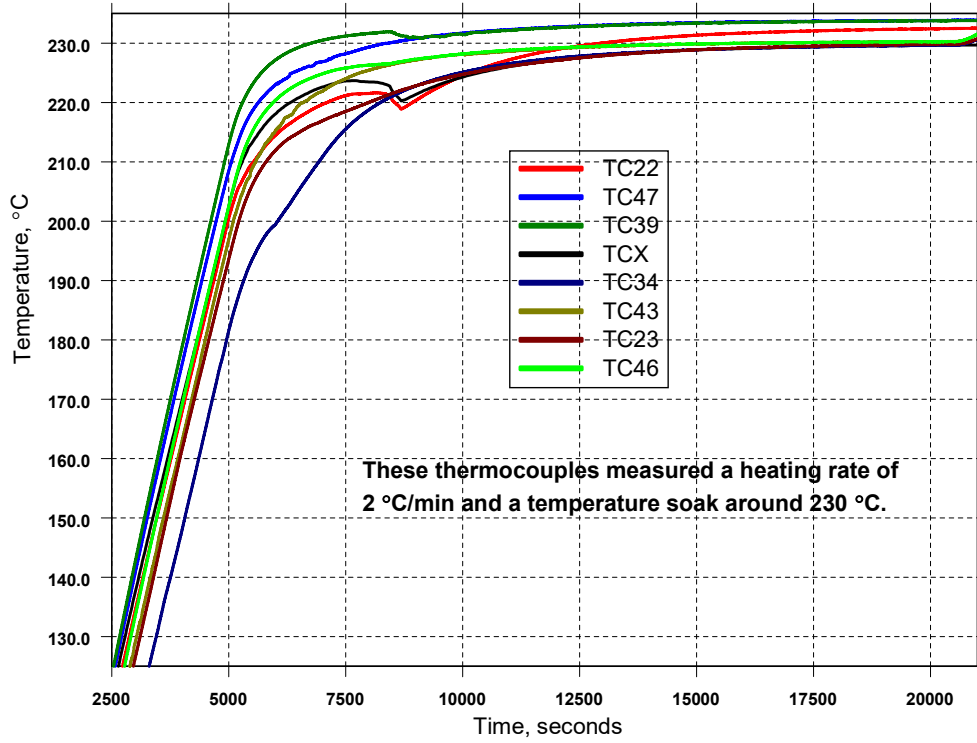

Figure 30. Heating rates and soak temperatures measured by the thermocouples installed at the equator of the steel confinement spherical cavity for the LT-55-1 and LT-55-2 experiments. See Figs. 16 and 25 for specific locations.

The FE prediction errors shown in Fig. 29 in the interval $0 \leq t \leq 13000$ s can be reduced by the estimation of the PBX surface temperatures T_5, T_6, T_7, and T_8 at the locations shown in Fig. 25. The first estimate of the functions T_5 and T_7 can be obtained using the same computational procedure developed previously to estimate the surface temperatures T_1, T_2, T_3, and T_4 in the simulations of the LT-55-1 experiment. The first estimate of T_6 was calculated assuming that the thermal conductances at the interface locations 47–6 (Fig. 25) and 43–2 (Fig. 16) are approximately equal. Note that this is a reasonable assumption because the first heating ramps for the LT-55-1 and LT-55-2 experiments were similar and as a consequence of this similarity, the thermal conditions at these interface locations were also similar. Also, the validity of this assumption can be reinforced by calculating the FE prediction error at the thermocouple 41 location. The energies in the form of heat coming into locations 2 and 6 shown in Figs. 16 and 25 respectively can be expressed as

$$q_2 = h_{43-2} \left(T_{43} - T_2 \right) A \tag{53}$$

28

$$q_6 = h_{47-6}\left(T_{47} - T_6\right)A \tag{54}$$

where h_{43-2} and h_{47-6} are the thermal conductances at the interface locations 43–2 (Fig. 16) and 47–6 (Fig. 25) respectively. Dividing Eq. (53) by $A\,T_2\,h_{43-2}$ and Eq. (54) by $A\,T_6\,h_{47-6}$ one gets

$$\frac{q_2}{A\,h_{43-2}\,T_2} = \left(\frac{T_{43}}{T_2} - 1\right) \tag{55}$$

$$\frac{q_7}{A\,h_{47-6}\,T_6} = \left(\frac{T_{47}}{T_6} - 1\right) \tag{56}$$

assuming that the dimensionless quantities appearing on the left hand sides of Eqs. (55) and (56) are approximately equal $q_2/(A\,h_{43-2}\,T_2) \approx q_7/(A\,h_{47-6}\,T_6)$, a first estimate of T_6 is obtained as

$$T_6 = \frac{T_{47}}{T_{43}}\,T_2 \qquad \text{for } 0 \le t \le 13000 \text{ s} \tag{57}$$

where T_2 was already estimated using the inverse procedure applied to calculate PBX outer surface temperatures for experiment LT-55-1. A first estimate for the surface temperature T_8 can also be obtained applying the same arguments used to obtain T_6. The energies in the form of heat coming into locations 4 and 8 shown in Figs. 16 and 25 respectively can be expressed as

$$q_4 = h_{46-4}\left(T_{46} - T_4\right)A \tag{58}$$
$$q_8 = h_{39-8}\left(T_{39} - T_8\right)A \tag{59}$$

where h_{46-4} and h_{39-8} are the thermal conductances at the interface locations 46–4 (Fig. 16) and 39–8 (Fig. 25) respectively. Dividing Eq. (58) by $A\,T_4\,h_{46-4}$ and Eq. (59) by $A\,T_8\,h_{39-8}$, the resulting equations read

$$\frac{q_4}{A\,h_{46-4}\,T_4} = \left(\frac{T_{46}}{T_4} - 1\right) \tag{60}$$

$$\frac{q_8}{A\,h_{39-8}\,T_8} = \left(\frac{T_{39}}{T_8} - 1\right) \tag{61}$$

assuming that the dimensionless quantities appearing on the left hand sides of Eqs. (60) and (61) are approximately equal $q_4/(A\,h_{46-4}\,T_4) \approx q_8/(A\,h_{39-8}\,T_8)$, a first estimate of T_8 reads

$$T_8 = \frac{T_4}{T_{46}}\,T_{39} \qquad \text{for } 0 \le t \le 13000 \text{ s} \tag{62}$$

A first estimate for T_5 and T_7 can be obtained approximating the energies flowing into locations 37 and 30 as one dimensional quantities

$$q|_{37} = \frac{4\pi k\,(T_{35} - T_{37})}{(1/R_1) - (1/R_2)} \tag{63}$$

$$q|_{30} = \frac{4\pi k\,(T_{38} - T_{30})}{(1/R_1) - (1/R_2)} \tag{64}$$

where T_{35}, T_{37}, T_{38}, and T_{30} are the thermocouple measurements at positions 35, 37, 38, and 30 shown in Fig. 23, k is the thermal conductivity of PBX 9502 [7] evaluated at the average temperature between R_1 and R_2, R_1 = 2 in, and R_2 = 2.75 in. The radial locations R_1 and R_2 are shown in Fig. 23. A first approximation to the surface temperatures T_5 and T_7 can be obtained assuming that $q|_{37} \approx q|_5$ and $q|_{30} \approx q|_7$. Under these assumptions, approximate expressions for the surface temperatures T_5 and T_7 are obtained as

$$T_5^1 = T_{37} - \frac{q|_5\,(R_0 - R_2)}{4\pi k\,R_0\,R_2} \qquad \text{for } 0 \le t \le 13000 \text{ s} \tag{65}$$

$$T_7^1 = T_{30} - \frac{q|_7\,(R_0 - R_2)}{4\pi k\,R_0\,R_2} \qquad \text{for } 0 \le t \le 13000 \text{ s} \tag{66}$$

where R_0 is the outer radius of the PBX (3 in), the superscript 1 in Eqs. (65) and (66) is used to imply that they represent the first guess for the surface temperatures. An iterative procedure was carried out to estimate the surface temperatures T_5 and T_7 in the interval $0 \le t \le 13000$ s. The first iteration step involves an FE simulation that uses Eqs. (57), (62), (65) and (66) as boundary conditions at locations 5, 6, 7, and 8 shown in Fig. 25. The rest of the boundary temperatures used for this simulation are the temperatures measured by the thermocouples shown in Figs. A3 and A4 with the exclusion of TC 22, TC 39, and TC 47. It is pointed out that the surface temperatures T_6 and T_8 given by Eqs. (57) and (62) are not modified by this iteration procedure. The functions T_6 and T_8 are not modified to see which is the effect of the estimation of T_5 and T_7 on the FE model prediction errors of the temperatures at locations 37, 35, 41, 38, and 30 in the mid-plane shown in Fig. 23. This first iteration produces the FE model predicted temperatures $T_{\text{fe}37}^1$ and $T_{\text{fe}30}^1$ at thermocouple locations 37 and 30 respectively. The second iteration corrects the surface temperatures calculated with Eqs. (65) and (66) as

$$T_5^2 = \frac{T_{37}}{T_{\text{fe}37}^1} T_5^1 \quad \text{for } 0 \le t \le 13000 \text{ s} \tag{67}$$

$$T_7^2 = \frac{T_{30}}{T_{\text{fe}30}^1} T_7^1 \quad \text{for } 0 \le t \le 13000 \text{ s} \tag{68}$$

where T_{37} and T_{30} are the thermocouple measurements at the mid-plane locations 37 and 30 respectively. The surface temperatures T_5^1 and T_7^1 used in the previous iteration are replaced with the corrected surface temperatures T_5^2 and T_7^2 and the FE model is run again using these surface temperatures as boundary conditions. Figure 31 shows the FE model prediction errors at the mid-plane locations 37, 35, 41, 38, and 30 that result from this second iteration. Note from Fig. 31
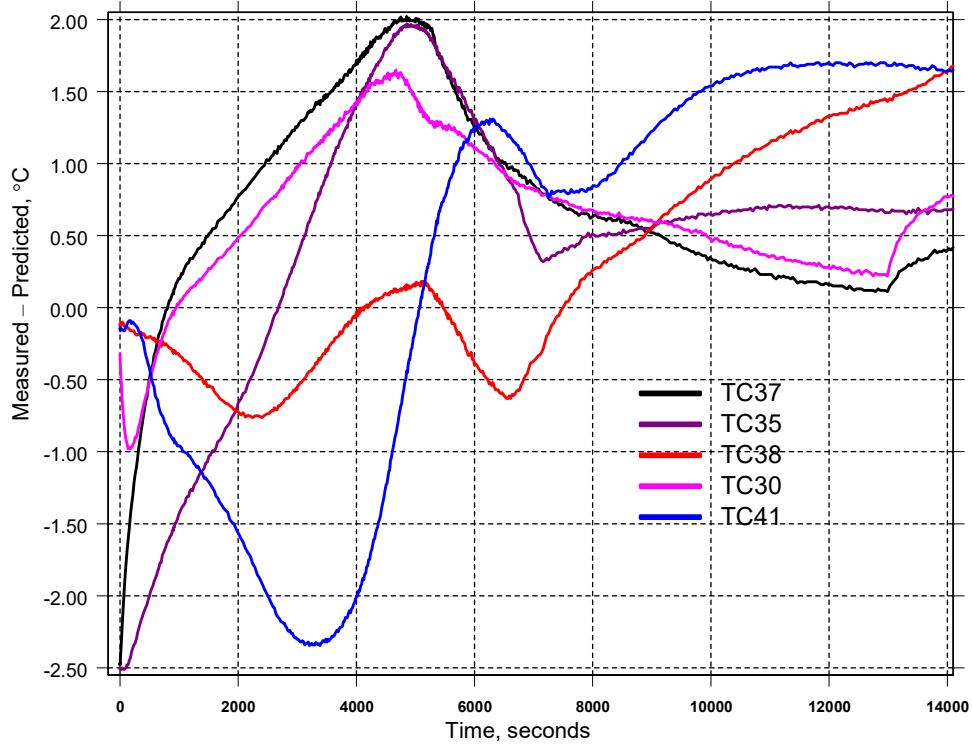
30

Figure 31. Errors associated with the estimation of functions $T_5^2(t)$, $T_7^2(t)$, $T_6(t)$, and $T_8(t)$ defined by Eqs. (67), (68), (57), and (62) respectively.

that the FE prediction errors fluctuate between –2.5 °C and +2 °C in the interval $0 \le t \le 13000$ s. For this reason, no additional iterations are carried out. Also, note that the assumptions made to obtain Eqs. (57) and (62) can be considered good approximations to the extent needed to predict the temperatures at the mid-plane. For example, the estimated temperature $T_6(t)$ has a significant effect on reducing the error at TC 41 since the vertical distance between locations 6 and 41 is only 2.5 cm. Notice that the magnitude of the maximum error for the FE prediction at TC 41 in Fig. (29) is –24 °C and the FE prediction at TC 41 fluctuates between –2.3 °C and +1.7 °C in Fig. 31. A comparison of Figs. (29) and (31) show that the FE prediction errors at locations 37 and 30 were also reduced significantly by the function estimation that lead to Eqs. (57), (62), (67), and (68).

The FE model of the PBX sphere was run to thermal ignition using the estimated surface temperatures $T_5^2(t)$, $T_7^2(t)$, $T_6(t)$, and $T_8(t)$ in the interval $0 \le t \le 13000$ s. For the other locations on the outer surface of the PBX, the temperatures measured by thermocouples shown in Figs. A3 and A4 were used in the interval $0 \le t \le 13000$ s. For times greater than 13000 s, the boundary conditions were defined using the temperatures measured by the thermocouples shown in Figs. A3 and A4. Also, Eq. (52) was used to replace the missing thermocouple for $t > 13000$ s. The FE model implemented with these surface temperatures predicted thermal ignition in 50934 s. Figure 32 shows the FE prediction errors in the mid-plane for this model which accounts for the presence of the air gap. The original model that uses only the temperature readings from the thermocouples shown in Figs. A3 and A4, and Eq. (52) as boundary conditions
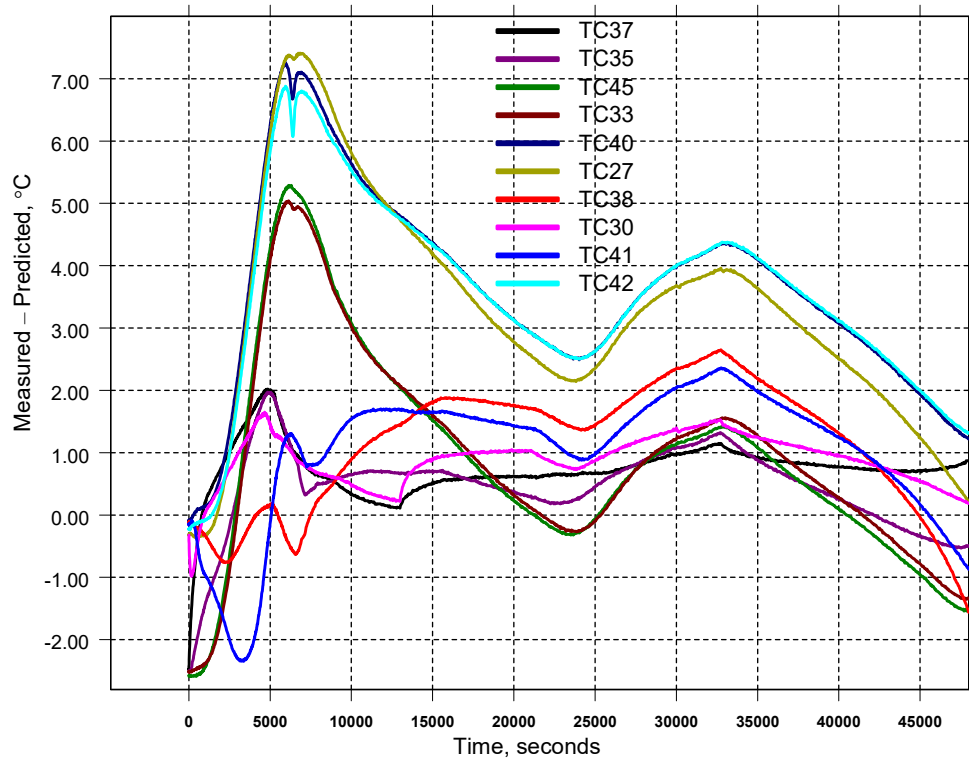
31

Figure 32. Finite element model prediction errors at the thermocouple locations shown in Fig. 23 using a pressure ratio exponent of 0.239 in Eq. (10). This model accounts for the air gap at the interface between the metal and the PBX.

predicted ignition in 50822 s. These predictions differ only by –0.2%. This shows that the presence of the air gap at the beginning of the experiment doesn't have a significant influence on the predicted times to thermal ignition. Figure 32 shows that the error fluctuates between –2.5 °C and +2.6 °C for thermocouples 37, 35, 38, 30, 41, and 42. The FE predictions have larger errors at the thermocouples 27, 40, 42, 45 and 33 locations. These are the thermocouples that are closer to the center of the PBX. Note from Fig. 18 that the FE predictions for the LT-55-1 experiment also have the largest errors at the thermocouple locations that are closer to the center of the PBX sphere. This is an indication that the mid-plane thermocouple measurements might have experienced conduction errors for the LT-55-1 and LT-55-2 experiments. The insertion of thermocouple wires across multiple isotherms creates paths for conduction heat transfer in the axial direction of the thermocouple wires. This is especially true if the thermal conductivity of the thermocouple wire is higher than the thermal conductivity of the material where temperature is being measured. Thermocouples of type-K were also used for this experiment. The metal wires for these thermocouples have a thermal conductivity of 30 W/m K. Also, the average thermal conductivity of PBX 9502 is 0.54 W/m K and the ratio of thermal conductivities between the wire and the PBX is 30/0.54 = 55.5 which shows that the thermal conductivity of the wire is at least 55 times larger than the conductivity of the PBX. This difference and a significant temperature gradient between the outer surface of the PBX and the point of measurement in the mid-plane have the potential to cause significant conduction measurement errors. Also, the

thermal contact conductance between the thermocouple wires sheath and its surrounding environment plays a significant role on the increase of the thermocouple conduction error.

A simple model for thermocouple conduction measurement error

Thermocouple measurement errors due to heat conduction have been investigated previously in the literature. A few examples are mentioned here. Reference [11] developed a model for predicting systematic temperature measurement errors due to thermal disturbances surrounding the thermocouple. Also, reference [12] considered errors in temperature measurements due to conduction along the sensor leads. Additional examples are described in refs. [13] and [14]. The objective here is to construct a simple FE model that can be used to estimate the order of magnitude of the temperature measurement conduction error that might develop in the thermocouples used to measure the temperature at the mid-plane shown in Figs. 11 and 23. The thermocouples used to measure the temperatures at the mid-plane have a part number: KMQLX-010U-24 (Omega ®) [15]. According to this part number, the thermocouples used have the configuration shown in Fig. 33 [16].
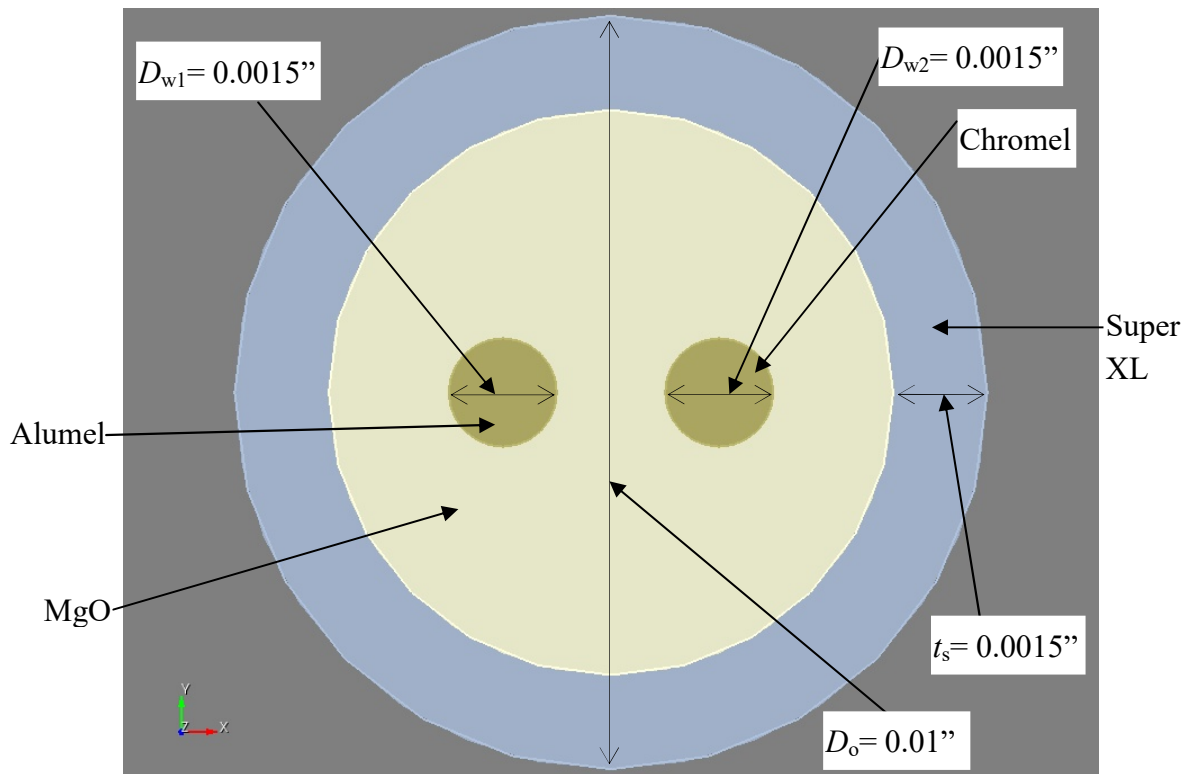

Figure 33. Configuration for thermocouple part number: KMQLX-010U-24 (Omega ®). Super XL is a proprietary Nickel alloy similar to Inconel alloy 600.

The above configuration shows that the diameters of both wires are the same. This allows for a simple simplification of this configuration. In order to obtain an axi-symmetric geometry, a single wire is considered located at the center of the MgO region. The area of cross section of the equivalent wire should be twice the area of either wire. That is $A_{w1}+A_{w2} = A_{we}$ where A_{w1} is the cross sectional area of wire 1, A_{w2} is the cross sectional area of wire 2, and A_{we} is the cross

sectional area of the equivalent wire. From this, one obtains that $\pi r_{w1}^2 + \pi r_{w1}^2 = \pi r_{we}^2$, and $r_{we} = \sqrt{2}\, r_{w1}$. The thermal resistances of the wires with length l are given as: $R_{w1} = l/(k_{w1}\, A_{w1})$, $R_{w2} = l/(k_{w2}\, A_{w2})$, and $R_{we} = l/(k_{we}\, A_{we})$ were k_{w1}, k_{w2}, and k_{we} are the thermal conductivities of wire 1, wire 2, and the equivalent wire respectively. For a thermal resistance network in parallel, one has that: $1/R_{we} = 1/R_{w1} + 1/R_{w2}$. Substituting the expressions for the thermal resistances and solving for k_{we} one gets that $k_{we} = (k_{w1} + k_{w2})/2$. Figure 34 shows the simplified configuration for this thermocouple.
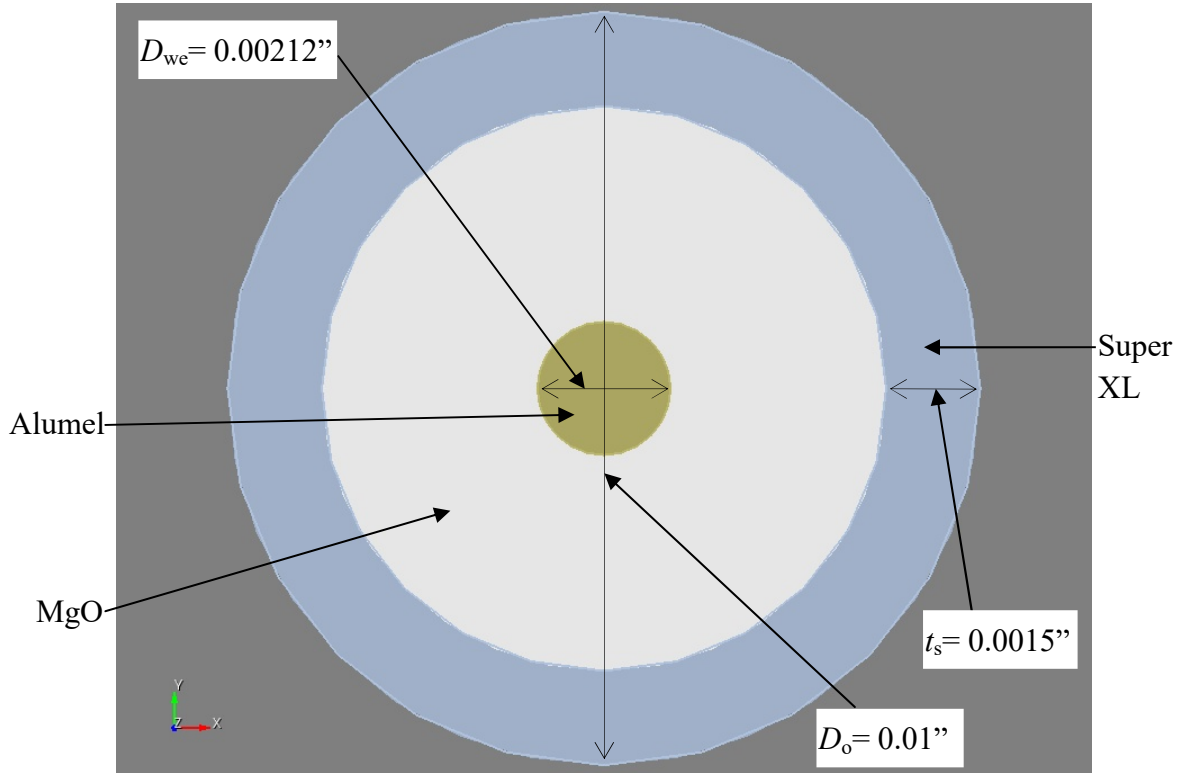

Figure 34. Simplified configuration for thermocouple part number: KMQLX-010U-24 (Omega ®). Super XL is a proprietary Nickel alloy similar to Inconel alloy 600.

An axisymmetric thermal model of a composite that involves a cylinder of PBX 9502 with a thermocouple embedded in its center is considered. This thermocouple has the same design as the one shown in Fig. 34. One of the objectives is to apply the temperature function estimated by Eq. (67) as a time dependent boundary condition at the bottom of this cylindrical composite. Figure 35 shows the details of this composite cylinder model. The intention is to subject the thermocouple shown in Fig. 34 to a thermal disturbance that is similar to the thermal disturbances experienced by the thermocouples installed at the mid-plane shown in Fig. 23. This is accomplished by applying Eq. (67) as a temperature boundary condition at the surface $z = 0$ in the model shown by Fig. 35. Also, the height of this composite cylinder is assumed to have the same value as the outer radius of the top and bottom spherical hemispheres shown in Fig. 4. This allows making temperature comparisons between the center of the wire and the $r = r_3$ interface for a height that has the same size as the distance between thermocouple 40 and the outer surface
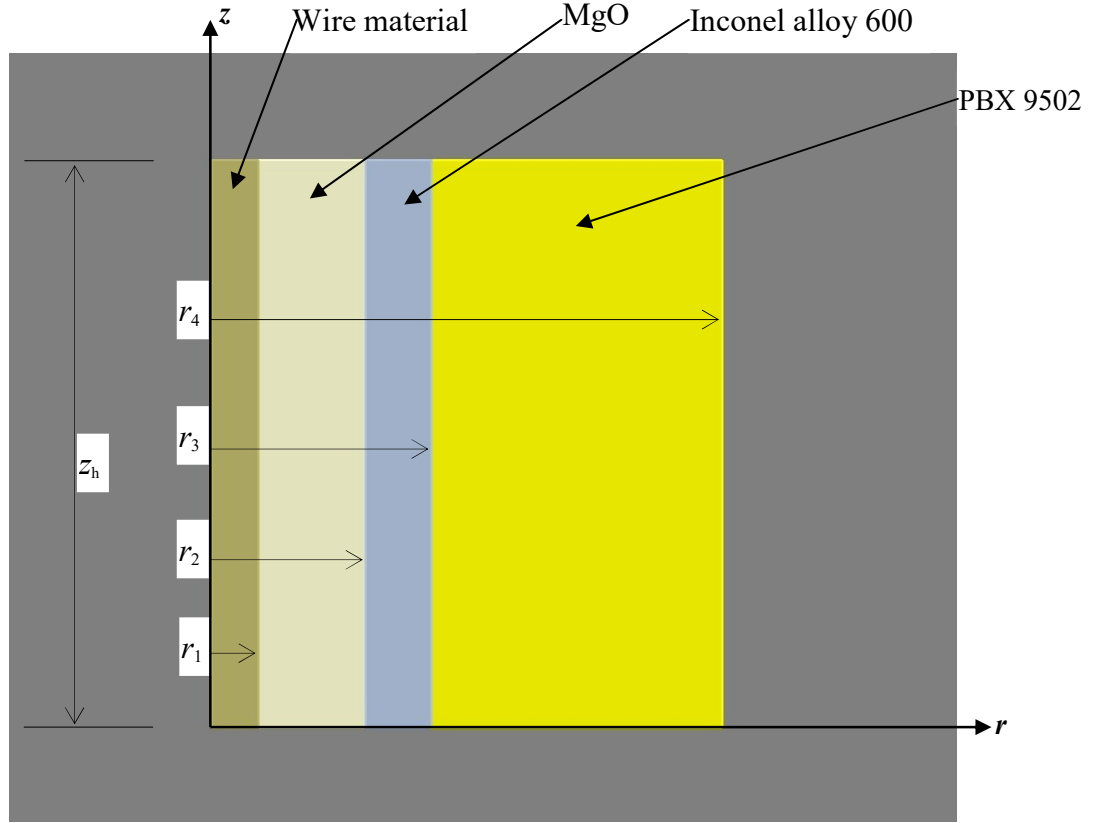
Figure 35. Axi-symmetric model used to estimate the order of the thermocouple measurement error due to heat conduction along the thermocouple wires.

of the PBX 9502 sphere. Temperature comparisons can also be made at other thermocouple locations shown in Fig. 23. Another parameter that influences the temperature difference between the center of the wire and the $r = r_3$ interface (on the PBX 9502 side) is the thermal contact conductance between the outer surface of the thermocouple sheath and the PBX 9502. Thermal resistance between the thermocouple sheath and its surroundings exists because there are 10 thermocouples inserted in the mid-plane between the top and bottom PBX 9502 hemispheres (see Figs. 4 and 23) and the outer diameter of the sheaths of these thermocouples is 0.01". The presence of these thermocouples creates a 0.01" gap that is filled with air at the beginning of the experiment. The size of this gap decreases some time after the first temperature ramp is applied because of the PBX 9502 thermal expansion effects. The parameters that define the size of the model shown in Fig. 35 are given in Table 2. The heat conduction equation is solved in each layer of this model. For the 4 layers in Fig. 35 one has

$$k_{we}\left[\frac{1}{r}\frac{\partial}{\partial r}\left(r\frac{\partial T_{a1}}{\partial r}\right) + \frac{\partial^2 T_{a1}}{\partial z^2}\right] = \rho_{we}c_{we}\frac{\partial T_{a1}}{\partial t} \qquad \text{for } 0 < r < r_1 \qquad (69)$$

$$\left[\frac{1}{r}\frac{\partial}{\partial r}\left(k_{\text{MgO}}\ r\ \frac{\partial T_{a2}}{\partial r}\right)+\frac{\partial}{\partial z}\left(k_{\text{MgO}}\ \frac{\partial T_{a2}}{\partial z}\right)\right]=\rho_{\text{MgO}}c_{\text{MgO}}\ \frac{\partial T_{a2}}{\partial t}\qquad\text{for }r_1<r<r_2 \qquad (70)$$

$$\left[\frac{1}{r}\frac{\partial}{\partial r}\left(k_{\text{inc}}\ r\ \frac{\partial T_{a3}}{\partial r}\right)+\frac{\partial}{\partial z}\left(k_{\text{inc}}\ \frac{\partial T_{a3}}{\partial z}\right)\right]=\rho_{\text{inc}}c_{\text{inc}}\ \frac{\partial T_{a3}}{\partial t}\qquad\text{for }r_2<r<r_3 \qquad (71)$$

$$\left[\frac{1}{r}\frac{\partial}{\partial r}\left(k\ r\ \frac{\partial T_{a4}}{\partial r}\right)+\frac{\partial}{\partial z}\left(k\ \frac{\partial T_{a4}}{\partial z}\right)\right]=\rho_{b}c_{b}\ \frac{\partial T_{a4}}{\partial t}\qquad\text{for }r_3<r<r_4 \qquad (72)$$

Table 2. Dimensions of model in Fig. 35.

Symbol in Fig. 35	Size in mm
r_1	0.0269
r_2	0.0889
r_3	0.127
r_4	40
z_h	76.2

where ρ_{we} and $c_{p\text{we}}$ are the density and heat capacity of the equivalent wire material respectively. The thermal properties of the equivalent wire material were taken from [17]. Also, k_{MgO}, ρ_{MgO}, and c_{MgO} are the thermal conductivity, density, and heat capacity of magnesium oxide respectively and were taken from reference [18]. For the Inconel alloy 600 layer, k_{inc}, ρ_{inc}, and c_{inc} are the thermal conductivity, density, and heat capacity respectively and were found in reference [19]. The thermal properties of the PBX 9502 layer were defined previously after the statement of Eq. (30) and were taken from ref. [7]. Since the MgO insulation is compacted between the wires and the metal sheath, it is assumed that the continuity of temperature and heat flux holds at the surfaces $r=r_1$ and $r=r_2$. This implies that

$$k_{\text{we}}\frac{\partial T_{a1}}{\partial r}=k_{\text{MgO}}\frac{\partial T_{a2}}{\partial r}\ ,\ T_{a1}=T_{a2}\quad\text{at }r=r_1 \qquad (73)$$

$$k_{\text{MgO}}\frac{\partial T_{a2}}{\partial r}=k_{\text{inc}}\frac{\partial T_{a3}}{\partial r}\ ,\ T_{a2}=T_{a3}\quad\text{at }r=r_2 \qquad (74)$$

Also, it is assumed that thermal contact resistance is present at the interface between the thermocouple metal sheath and the PBX 9502. This assumption is made to associate this problem with the thermal conditions experienced by the thermocouples installed at the mid-plane shown in Fig. 23. This condition is modeled considering a thermal contact conductance that is a function of the height in the z direction. A "gap" flux is defined across the interface proportional to the temperature drop,

$$-k_{\text{inc}}\frac{\partial T_{a3}}{\partial r}\bigg|_{r=r_3}=h_c\left(T_{a3}\big|_{r=r_3}-T_{a4}\big|_{r=r_3}\right)=-k\frac{\partial T_{a4}}{\partial r}\bigg|_{r=r_3} \qquad (75)$$

36

where h_c is the contact conductance which is a function of z. In order to get an estimate of the contact conductance function h_c, a generic thermocouple is assumed to be installed along the radial line where thermocouple 37 is located in Fig. 23. It is also assumed that this thermocouple has a length equal to the outer radius of the PBX 9502 sphere and ends at the center of this sphere. Figure 36 shows a sketch of this situation. It is assumed that the effective thermal conductivity of the "gap" between the metal sheath and the outer surface of the PBX sphere is a constant denoted by k_{eff}. An estimate of the thermal resistance generated by this gap is given by
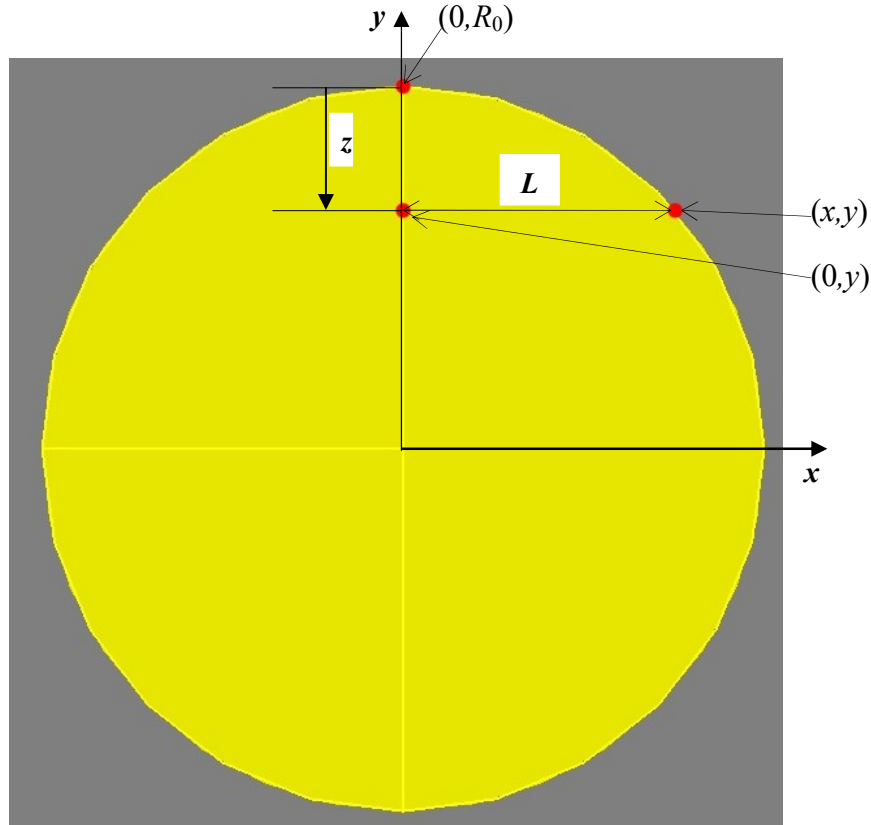

Figure 36. The thermocouple metal sheath is assumed to be located in a straight line between points $(0,R_0)$ and $(0,0)$. The length of the interface that this metal sheath is facing in the x direction is L.

$$R_x = \frac{L}{k_{eff}} \tag{76}$$

where L is the distance from the outer surface of the thermocouple metal sheath to the edge of the PBX hemisphere (see Fig. 36). Note from Fig. 36 that $L = x = \sqrt{R_0^2 - y^2}$ and $R_0 - y = z$. From this, a simple expression for the contact conductance h_c can be obtained from Eq. (76) as

$$h_c = \frac{k_{eff}}{\sqrt{2 R_0 \, z - z^2}} \tag{77}$$

A temperature boundary condition given by Eqs. (67) (for $0 \leq t \leq 1300$ s) and (52) (for $t > 13000$ s) is applied at the surface $z = 0$. The rest of the surfaces are assumed to be insulated. As mentioned previously, the difference between the temperature at the center of the wire and the $r = r_3$ interface (on the PBX 9502 side) is calculated at different heights in the composite. This difference is intended to represent the thermocouple heat conduction measurement error at these locations. Figure 37 shows a schematic representation of the temperature differences probed from this model. The symbols ΔT_{45}, ΔT_{33}, and ΔT_{40} are meant to associate the estimated errors with thermocouples 45, 33, and 40 (shown in Fig. 23) respectively. Table 3 lists the values of the probing heights shown in Fig. 37.
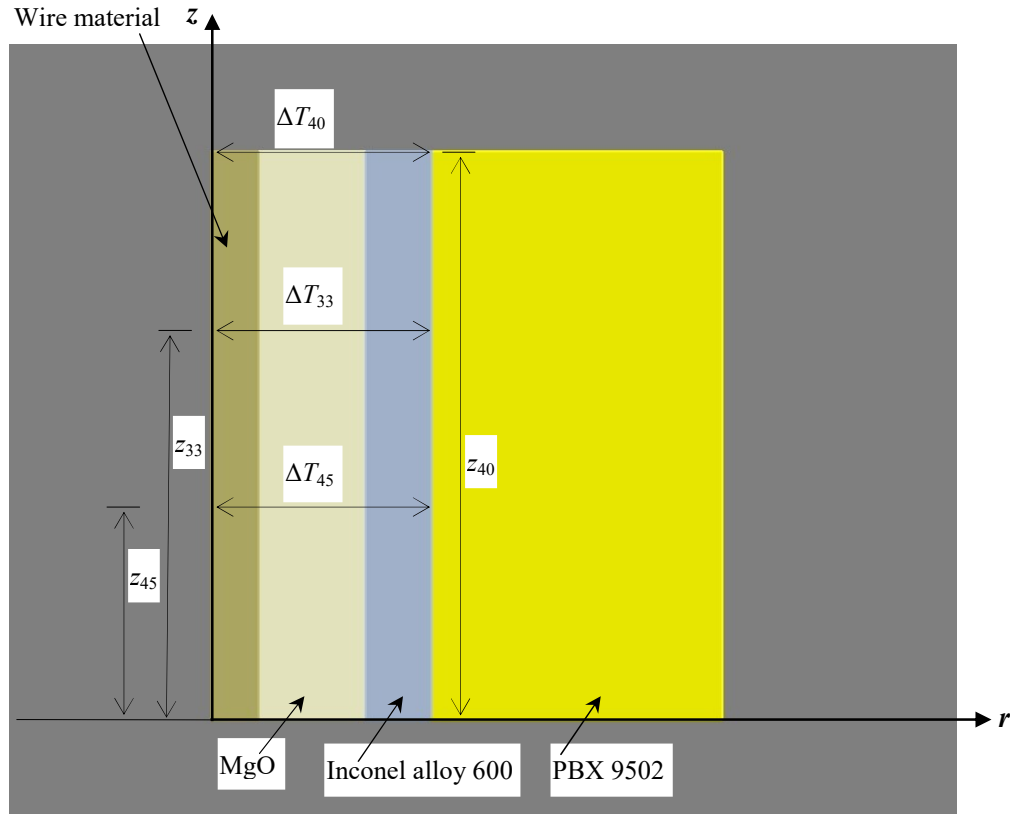

Figure 37. Schematic of the association of the composite thermocouple model with thermocouple locations 45, 33, and 40 shown in Fig. 23. The symbols z_{45}, z_{33}, and z_{40} are the distances from the outer surface of the PBX sphere to the thermocouple locations 45, 33, and 40 respectively.

Table 3. Probing heights in Fig. 37

Symbol in Fig. 37	Size in mm
z_{45}	57.09
z_{33}	65.14
z_{40}	76.20

Since Eq. (77) is singular at $z = 0$, the contact conductance was defined as a constant for $z \leq 0.00635$ m, and for $z > 0.00635$ m Eq. (77) was used to define the conductance. Parametric studies involving k_{eff} were made to match the order of magnitude of the error shown by TC 40 in Fig. 32. The function found has the form

$$h_c = \begin{cases} 23.35 & \text{for } z \leq 0.00635 \text{ m} \\ \dfrac{0.711}{\sqrt{2\,R_0\,z - z^2}} & \text{for } z > 0.00635 \text{ m} \end{cases} \tag{78}$$

where h_c is given in W/m^2 K. The model represented by Eqs. (69)–(75) and (78) was implemented in the FE heat transfer code Aria [1]. Equation (78) was programmed in a C++ user subroutine which was used as a user plug-in to carry out these parametric studies. The range of conductance values spanned by Eq. (78) are given in Fig. 38. The results of the FE model that implements Eqs. (69)–(75) and (78) are given in Fig. 39.
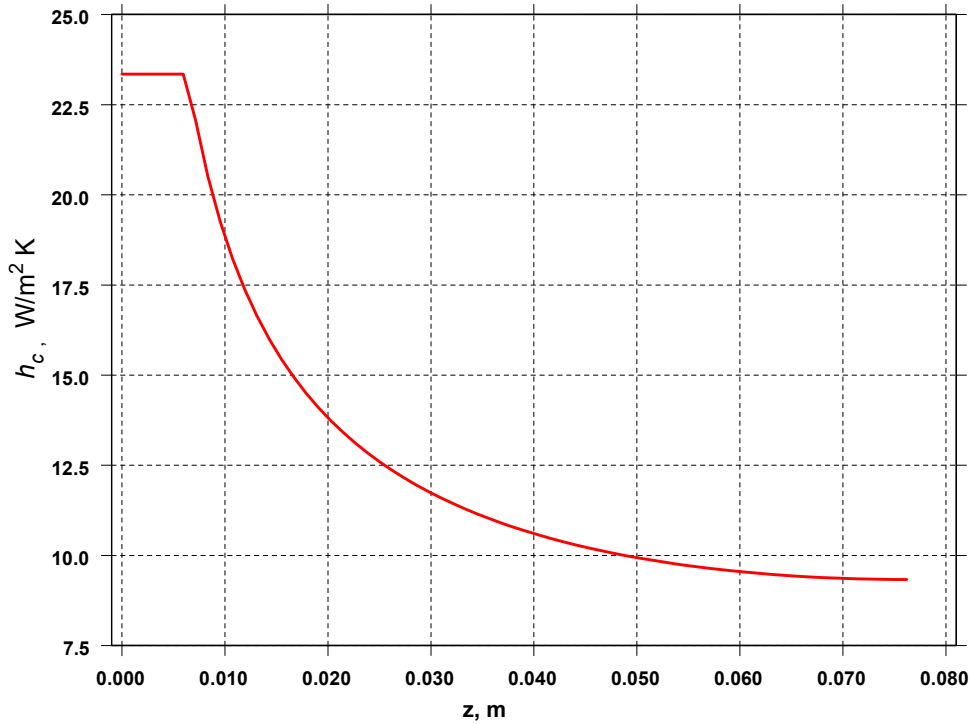

Figure 38. Range of conductance values spanned by Eq. (78) for different values of z up to the total length of thermocouple 40 sheath.

Note that the shape of the errors shown in Fig. 39 are similar to the errors calculated at thermocouple locations 45, 33, and 40 which are shown in Fig. 32. If the conductance between the outer surface of the thermocouple sheaths of TC 45, 33, and 40 and the PBX 9502 at the mid-plane is of the same order than the conductance defined by Eq. (78), a significant part of the errors shown in Fig. 32 for TC locations 45, 33, and 40 can be due to thermocouples conduction measurement errors. Also, note that the maximum differences predicted by this model take place
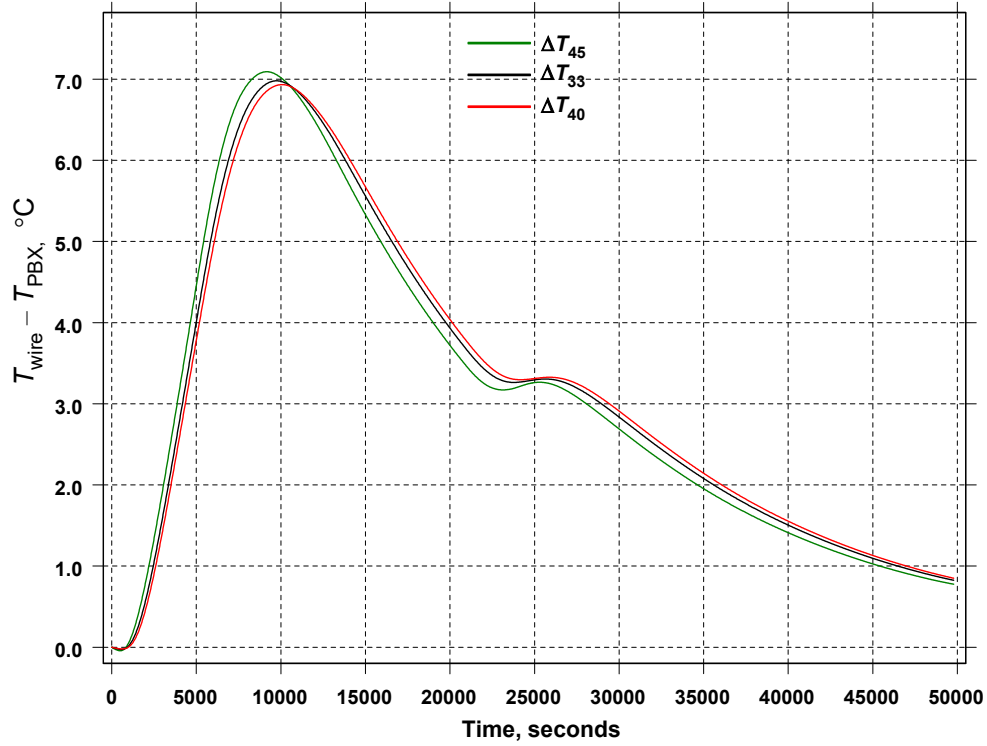
Figure 39. Temperature differences produced by FE model of Eqs. (69)–(75) and (78). The temperature boundary condition applied to this model is the surface temperature T_s^2 (Eq. 67) for $t \leq 13000$ s and Eq. (52) for $t > 13000$ s.

close to a time equal to 10000 s. This is the time when the PBX sphere (or the composite PBX cylinder) is experiencing the largest temperature gradients between its outer surface and its center. These gradients begin to decrease for times greater than 10000 s due to the temperature soak induced by the surface temperature T_x (Fig. 25). A plot of this surface temperature is shown in Fig. 30 as TCX. The errors in Fig. 39 begin to increase slightly around a time equal to 23800 s. Notice that this is the time when the second boundary temperature ramp ends for test 2 (see Fig. 7). The gradients created by this second ramp don't have a significant effect on the errors shown in Fig. 39 because the composite cylinder (or the PBX sphere) is already at a higher temperature and the magnitude of the temperature increase produced by the second ramp is less than 25 °C.

In order to get an estimate of the order of magnitude the thermocouples conduction error for the LT-55-1 test, a generic thermocouple is assumed to be located along the radial line where thermocouple 40 is located in Fig. 11. This assumption allows estimating the order of the conduction error for thermocouples 20 and 44 shown in Fig. 11. Since the first temperature ramps applied for the LT-55-1 and LT-55-2 experiments are similar (see Figs. 6 and 7) and the assembly procedure was practically the same, it is expected that the range of conductance values necessary to obtain an error magnitude like the one shown in Fig. 18 for TCs 20 and 44 should be similar to the range shown by Fig. 38. For this case, a time dependent temperature boundary condition represented by Eq. (39) for $t \leq 13000$ s and TC 34 for $t > 13000$ s is applied at the surface $z = 0$ of the composite thermocouple model shown in Fig. 35. The generic thermocouple is assumed to be located in a straight line between points $(0, R_0)$ and $(0,0)$ in Fig. 36. Parametric

40

studies were carried out using Eq. (77) to obtain a value of k_{eff} that produces a maximum temperature difference of ~5 °C. This temperature difference is about the same as the temperature differences between the FE model and TC 20 and TC 44 in Fig. 18. The function found has the form

$$h_c = \begin{cases} 33.12 & \text{for } z \leq 0.00635 \text{ m} \\ \dfrac{1.01}{\sqrt{2\, R_0\; z - z^2}} & \text{for } z > 0.00635 \text{ m} \end{cases} \tag{79}$$

where h_c is given in W/m^2 K. Figure 40 shows a schematic representation of the temperature differences probed from this model. The symbols ΔT_{20} and ΔT_{44} are meant to associate the estimated errors with thermocouples 20 and 44 (shown in Fig. 11) respectively. Figure 41 shows a plot of Eqs. (78) and (79). The results from this model are shown in Fig. 42. Note that the errors shown in Fig. 42 reach their maximums around 10000 s. This is also the case for TC 20 and TC 44 shown in Fig. 18. If the conductance between the outer surface of the thermocouple sheaths of TC 20 and TC 44 and the PBX 9502 at the mid-plane is of the same order as the conductance defined by Eq. (79), a significant part of the errors shown in Fig. 18 for TC 20 and TC 44 can be due to thermocouple conduction measurement errors.
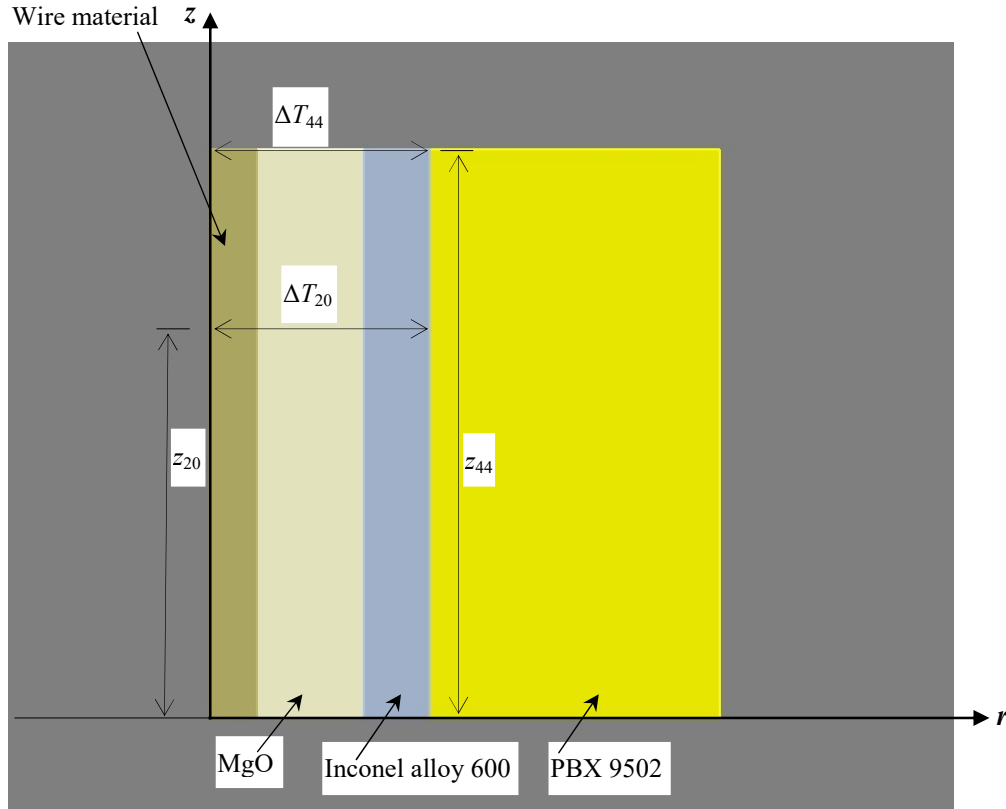

Figure 40. Schematic of the association of the composite thermocouple model with thermocouple locations 20 and 44 shown in Fig. 11. The symbols z_{20} and z_{44} are the distances from the outer surface of the PBX sphere to the TC locations 20 and 44 respectively.
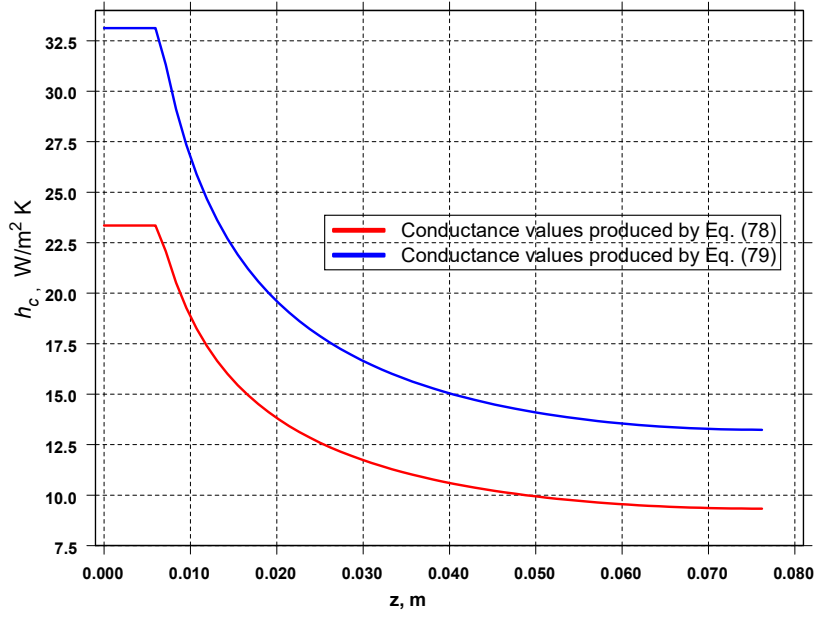
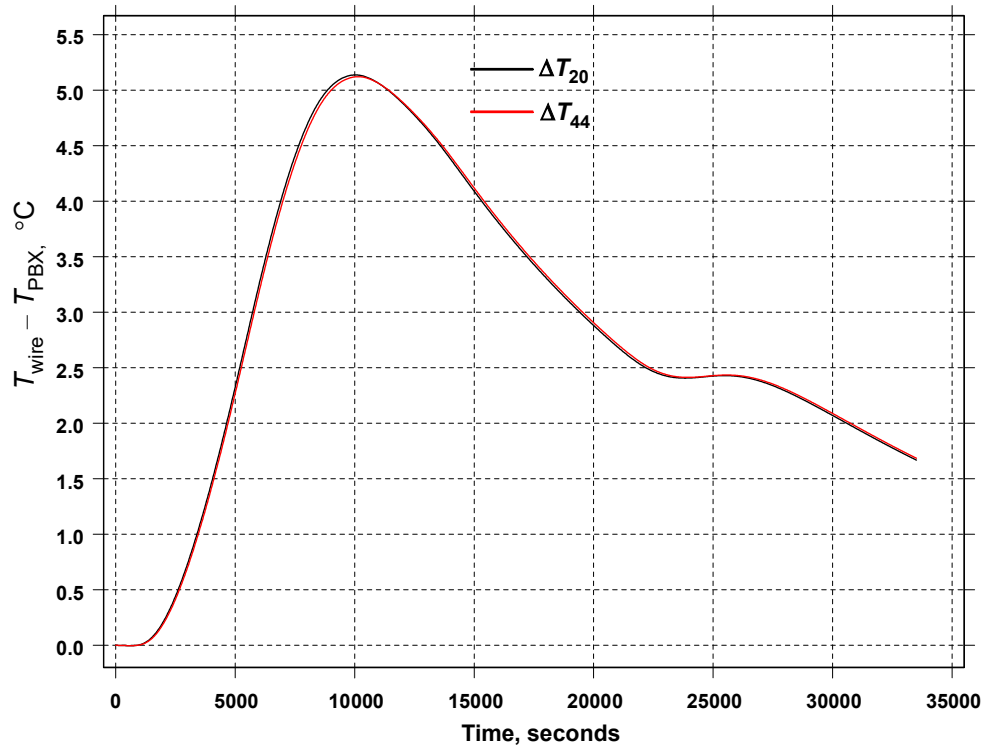Figure 41. Range of conductance values produced by Eqs. (78) and (79) from $z = 0$ to $z = z_h$.

Figure 42. Temperature differences produced by FE model of Eqs. (69)–(75) and (79). The temperature boundary condition applied to this model is the surface temperature T_1^2 (Eq. 39) for $t \leq 13000$ s and TC 34 for $t > 13000$ s.

This parametric study shows that the thermal resistance between the outer surface of the mid-plane thermocouple sheaths and the PBX 9502 sphere at the mid-plane plays a significant role in the development of thermocouple conduction error. The magnitudes of the temperature gradients between the outer surface of the PBX sphere (at the mid-plane) and its center are also very influential in developing the thermocouple conduction errors. Also, this study shows that the thermal conditions necessary for the development of thermocouple conduction error are present since the beginning of the LT-55-1 and LT-55-2 experiments and this error develops in the mid-plane thermocouples during the course of the temperature ramps that are applied first. The second temperature ramps are not influential in developing this error because the magnitudes of the temperature gradients produced by these ramps are not sufficiently large.

The effective thermal conductivities in Eqs. (78) and (79) contain the effects of two interfaces. The first interface is the one between the two PBX hemispheres mid-planes and has a variable length as shown in Fig. 36. The second interface is the one between the outer surface of the Inconel 600 thermocouple sheath and its immediate surroundings. Note that the surroundings of the outer surface of this thermocouple sheath are composed of two materials, PBX 9502 and air. As the PBX 9502 hemispheres expand during the first temperature ramps, the mid-planes from the upper and lower PBX hemispheres eventually come into contact creating an interface that contains voids filled with air. The effective thermal conductivity along this interface (in the x direction in Fig. 36) can be considered to be the one of a porous material. The porosity of this material can be defined as the volume of the voids filled with air divided by the total volume of this porous material and is designated as ε. The effective thermal conductivity of the first interface is designated as k_{porous} and can be approximated using the geometric mean of the thermal conductivities of air and PBX 9502. An expression that is commonly used in heat transfer in porous media [20] for this geometric mean has the form

$$k_{porous} = k_{air} \left(\frac{k}{k_{air}} \right)^{1-\varepsilon} \tag{80}$$

where k and k_{air} are the thermal conductivities of PBX 9502 and air respectively. Correlations for contact conductance [21] use the harmonic mean of the thermal conductivities of the two materials in contact. For the second interface, the harmonic mean is calculated as

$$k_{eff} = \frac{2\, k_{porous}\, k_{inc}}{k_{porous} + k_{inc}} \tag{81}$$

where k_{inc} is the thermal conductivity of the Inconel 600 alloy. Assuming an average temperature of 127 °C calculated between the initial temperature and the first temperature soak, the values of the thermal conductivities k, k_{air}, and k_{inc} are 0.536 W/m K, 0.0338 W/m K, and 20.5 W/m K respectively. Substituting these thermal conductivities into Eqs. (80) and (81), and assuming a porosity of 14 % ($\varepsilon = 0.14$), k_{eff} takes a value of 0.715 W/m K. This is almost the same value estimated in Eq. (78). Also, if the porosity ε in Eq. (80) is assumed to have a value of 3%, and the thermal conductivities k, k_{air}, and k_{inc} are 0.536 W/m K, 0.0338 W/m K, and 20.5 W/m K respectively, k_{eff} in Eq. (81) takes a value of 0.96 W/m K. Note that this is almost the same

value estimated in Eq. (79). These calculations help to explain the effective thermal conductivities found by iteration in Eqs. (78) and (79). Equation (80) has been used to correlate experimental measurements of effective thermal conductivities of porous materials. Examples of these applications are given in references [22] and [23].

It was necessary to run the FE model represented by Eqs. (69)–(75) and (78) in a super-computer because it contains 957154 quadrilateral elements with four integration points. The FE heat transfer code used is also called Sierra thermal/fluids [1] and it is part of the Sandia National Laboratories (SNL) Sierra codes framework which was designed to run in parallel computers. The Tri-Lab Capacity Clusters (TLCCs) "Moonlight" and "Wolf" located at LANL were used to run these calculations.

Conclusions and comments

This study shows that the PBX 9502 cook-off model developed by Hobbs et al. [3] can be applied to model systems that experience leakage of thermal decomposition gases by estimating the value of the exponent e of the pressure ratio that appears in Eq. (10) which defines reaction rate r_4 in step 4 of the PBX decomposition mechanism. Previously, this model has been validated [24] for the One-Dimensional Time to Explosion (ODTX), Sandia Instrumented Thermal Ignition apparatus (SITI), and Intermediate-Scale Cook-off Bucket (ISCB) experiments which contained 1.8 g, 24 g, and 1312 g of PBX 9502 respectively. These simulations also corroborate that Hobbs' et al. [3] model has predictive capabilities to simulate larger masses of PBX 9502 because the LT-55-1 and LT-55-2 experiments contained PBX 9502 spheres with a mass of ~3500 g.

It became necessary to develop and implement a computational scheme that was used to solve an inverse heat conduction problem which produced the surface temperatures at the mid-plane of the PBX spheres. This allowed the application of more realistic temperature boundary conditions to simulate the experiments. These boundary conditions produced a good agreement between the FE model and the internal temperature measurements carried out at the mid-plane which is shown in Figs. 18 and 32. A FE model for thermocouple conduction error was constructed and associated with the thermal conditions that the mid-plane thermocouple sheaths experienced in these experiments. The results from this model were used to assess the errors seen in Figs. 18 and 32. The PBX 9502 thermal properties estimated by Erikson et al. [7] which are part of the Hobbs et al. [3] cook-off model were used in these calculations.

The FE model of the PBX spheres was meshed with linear tetrahedral elements. This mesh contains 56088 elements and was used to carry out the simulations presented here. The FE model mesh was refined to see the effect of convergence on the calculated results. The refined mesh contains 1582482 elements and was used to simulate the LT-55-2 experiment. Figure 43 compares the results obtained from the original and refined meshes at the thermocouple locations shown in Fig. 23 using the boundary conditions from experiment LT-55-2. Note that the differences between these two models fluctuate between –0.3 °C and 0.16 °C with the exception of locations TC 37 and TC 30 which experience differences between 0.2 °C and 1.3 °C in the interval 884 s $\leq t \leq$ 11582 s. Notice that locations 30 and 37 are the ones closer to the outer surface of the sphere and that they are more sensitive to convergence. This is especially true for temperature boundary condition type cases. However, the differences calculated at locations 30 and 37 in the interval 884 s $\leq t \leq$ 11582 s are still within the order of the measurement accuracy of the thermocouples used which is equal to ±1.1 °C. A comparison between the mid-plane
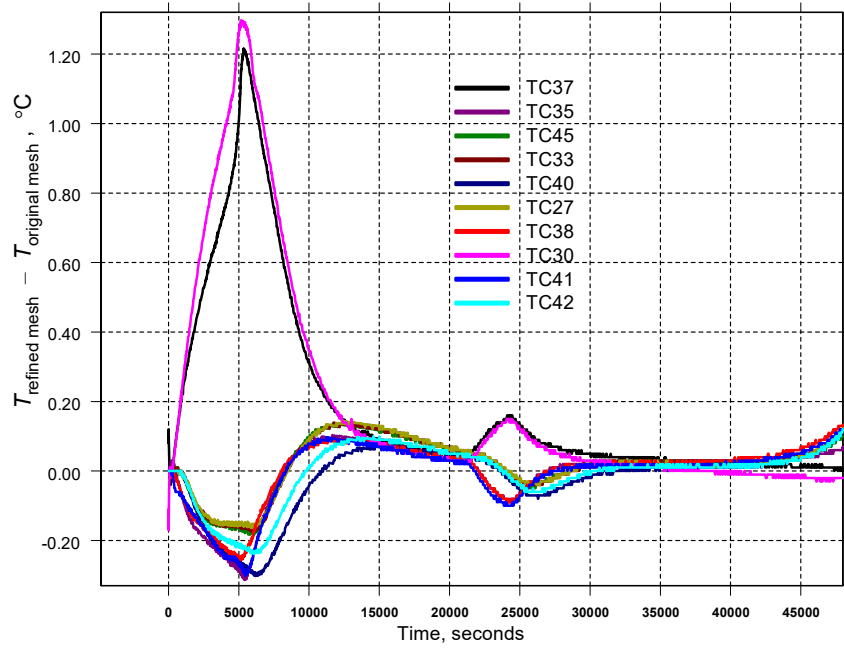
Figure 43. Comparison of the temperatures calculated with the FE models that use the original and refined meshes of the PBX sphere. The boundary conditions used in this comparison are the ones implemented for the LT-55-2 experiment. Models are evaluated at the Fig. 23 TC locations.
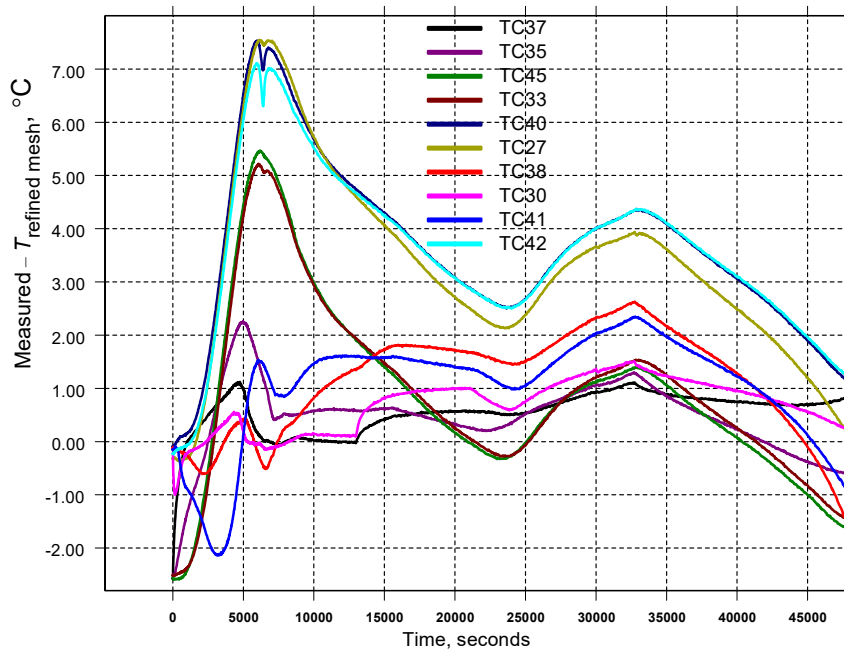

Figure 44. Comparison of the mid-plane temperatures measured for the LT-55-2 experiment with the temperatures predicted by the FE model that uses the refined mesh with the LT-55-2 boundary conditions.

temperatures calculated using the refined mesh and the temperature measurements at the mid-plane (Fig. 23) for the LT-55-2 experiment is shown in Fig. 44. An inspection of Figs. 32 and 44 reveals that the original mesh and the refined mesh produce practically the same results. This shows that the FE model used for the calculations presented here already contains a reasonable degree of convergence. It is pointed out that the C++ user subroutines that define the temperature on the outer surface of the PBX sphere were modified to run the refined mesh case.

Acknowledgements

References

[1] Notz, P. K., Subia, S. R., Hopkins, M. M, Moffat, H. K., Noble, D. R., "Aria 1.5: User Manual," Sandia Report SAND2007-2734, Sandia National Laboratories, P. O. Box 5800, Albuquerque, NM 87185, 2007.

[2] Parker, G. P., "Quick Look Report for Local Test-55-1 & -2: The Heavily Confined PBX 9502 Cookoff Tests." Memorandum to Distribution, Symbol: WX6-15-1570. Weapons Experiments Division, WX-6: HE Thermal and Mechanical Response Team, Los Alamos National Laboratory, Los Alamos NM, January 21, 2015.

[3] Hobbs, M. L. and Kaneshige, M. J., J. *Chem. Phys.* **140**, 124203 (2014).

[4] Hobbs, M. L. and Baer, M. R., *Shock Waves* 2, 177 (1992).

[5] Maienschein, J. L. and Garcia, F., *Thermochim. Acta* 384, 71 (2002).

[6] Gibbs, T. R. and Popolato, A., *LASL Explosive Property Data* (University of California Press, Berkeley, CA, 1980), p. 124.

[7] Erikson, W. W., Cooper, M. A., Hobbs, M. L., Kaneshige, M. J., Oliver, M. S., Snedigar, S., "Determination of thermal diffusivity, conductivity, and energetic release from internal temperature profiles of energetic materials," *International Journal of Heat and Mass Transfer*, **79** (2014) 676–688.

[8] Wichman, I. S., "On the Use of Operator-Splitting Methods for the Equations of Combustion," *Combust. Flame*, 83, 240-252, 1991.

[9] Young, T. R., "CHEMEQ–A Subroutine for Solving Stiff Ordinary Differential Equations," Tech. Rep NRL Memorandum Report 4091, Naval Research Laboratory, Washington D. C., 1980.

[10] Figliola, R. S. and Beasley, D. E., "*Theory and Design for Mechanical Measurements*," 2nd ed. , Copyright © 1995, by John Wiley & Sons, Inc.

[11] Attia, M. H., Cameron, A., Kops, L., "Distortion in Thermal Field Around Inserted Thermocouples in Experimental Interfacial Studies, Part 4: End Effect," ASME *Journal of Manufacturing Science and Engineering,* **124** (2002) 135-145.

[12] Singh, B. S., and Deybbs, A., 1976, ''Errors in Temperature Measurements due to Conduction Along the Sensor Leads,''ASME J. Heat Transfer, pp. 491-495.

[13] Moffat, R. J., ''Temperature Measurements in Solids: Errors Due to the Thermal Resistance Between the Thermocouple and the Specimen,'' Proceedings of the Symposium on Advances in Test Measurements, Vol. 5, No. 68-54, Pittsburgh, Pa.

[14] Sparrow, E. M., 1970, ''Errors Estimates in Temperature Measurements,'' AGARDograph No. 130, Measurement Techniques in Heat Transfer, E. R. Eckert and R. J. Goldstein, eds., pp. 13-32.

[15] Holmes, M. D. "Private Communication," M-6, Explosives Applications and Special Projects, Los Alamos National Laboratory, Los Alamos New Mexico 87545, May 2015.

[16] Omega Engineering, INC., "Private Communication," www.omega.com, Case # 177771, One Omega Drive P.O. Box 4047, Stamford, Connecticut 06907-0047, May 21, 2015.

[17] Omega Engineering, INC., www.omega.com, "Physical Properties of Thermoelement Materials," One Omega Drive P.O. Box 4047, Stamford, Connecticut 06907-0047.

[18] Slifka, A. J., Filla, B. J., and Phelps, J. M., "Thermal Conductivity of Magnesium Oxide From Absolute, Steady-State Measurements," *Journal of Research of the National Institute of Standards and Technology*, Volume 103, Number 4, July-August, 1998, National Institute of Standards and Technology, Boulder, CO 80303.

[19] Special Metals Corporation, www.specialmetals.com, "INCONEL® alloy 600," 3200 Riverside Drive, Huntington, West Virginia 25705, USA.

[20] Kaviany, M., "*Principles of Heat Transfer in Porous Media*," © 1995 Springer-Verlag New York, Inc., Fifth Avenue, New York, NY 10010, USA.

[21] Madhusudana, C. V., "*Thermal Contact Conductance*," © 1996 Springer-Verlag New York, Inc., Fifth Avenue, New York, NY 10010, USA.

[22] Kinoshita, M. "Estimation of Grain Thermal Conductivity in the Turbidite Sediment of the Juan de Fuca Ridge," Mottl, M.J., Davis, E.E., Fisher, A.T., and Slack, J.F. (Eds.), 1994. *Proceedings of the Ocean Drilling Program, Scientific Results*, 139: College Station, TX (Ocean Drilling Program).

[23] Fuchs, S., Schütz, F., Förster, H-J., Förster, A., "Evaluation of common mixing models for calculating bulk thermal conductivity of sedimentary rocks: Correction charts and new conversion equations," *Geothermics* 47 (2013) 40– 5.

[24] Aviles-Ramos, C., Hobbs, M. L., Parker Jr., G. R., Kaneshighe, M. J., and Holmes, M. D., "Validation of a Pressure Dependent PBX 9502 Cookoff Model," 15th International Detonation Symposium, San Francisco, CA, July 7, 2014 to July 18, 2014.
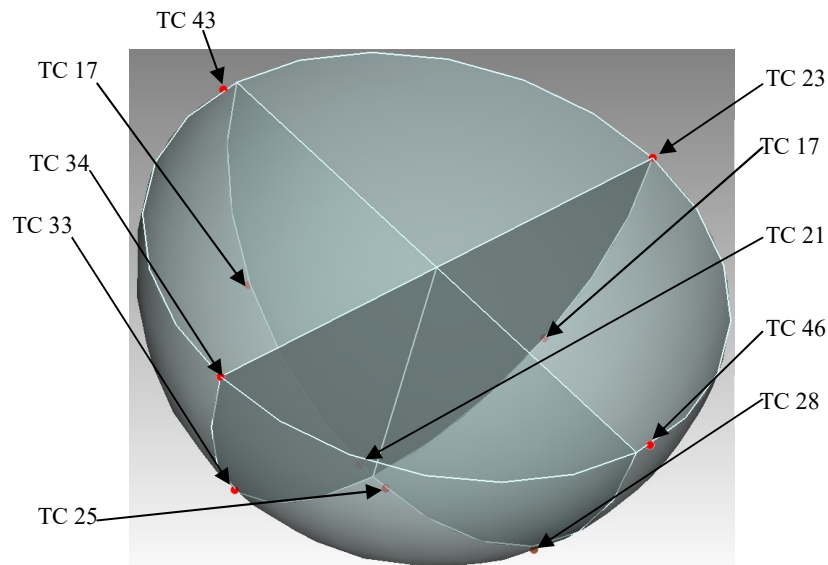
Appendix A

Figure A1. Thermocouples taped to the steel spherical cavity for the LT-55-1 test. The thermocouple numbering is defined in drawing No. TCLayout-Test1Metal-mapped.
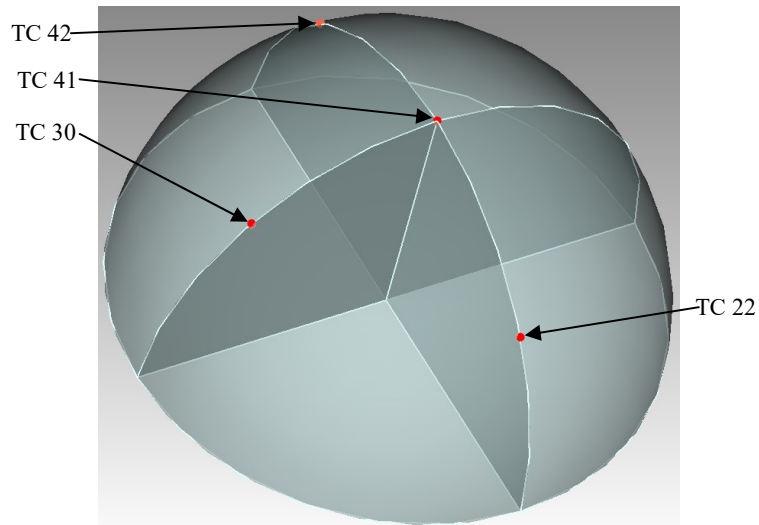
Figure A2. Thermocouples taped to the top PBX 9502 hemisphere for the LT-55-1 test. The thermocouple numbering is defined in drawing No. TCLayout-Test1HE-mapped. Thermocouple 35 (not shown) failed.
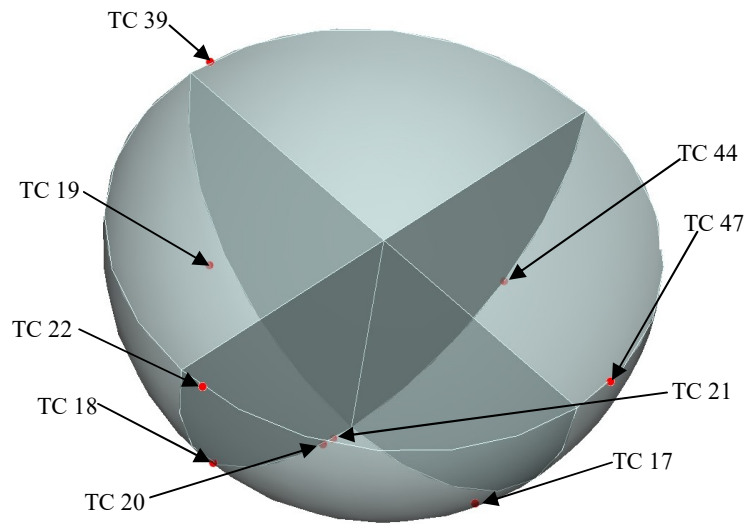

Figure A3. Thermocouples taped to the steel spherical cavity for the LT-55-2 test. The thermocouple numbering is defined in drawing No. TCLayout-Test2Metal-mapped.
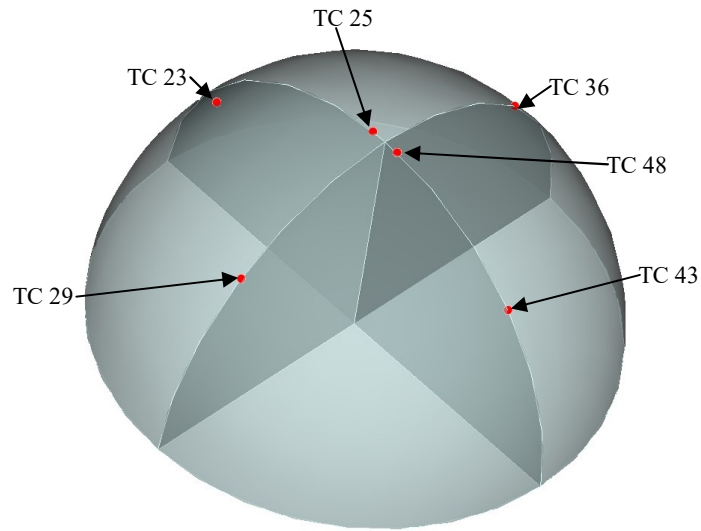
Figure A4. Thermocouples taped to the top PBX 9502 hemisphere for the LT-55-2 test. The thermocouple numbering is defined in drawing No. TCLayout-Test2HE-mapped.
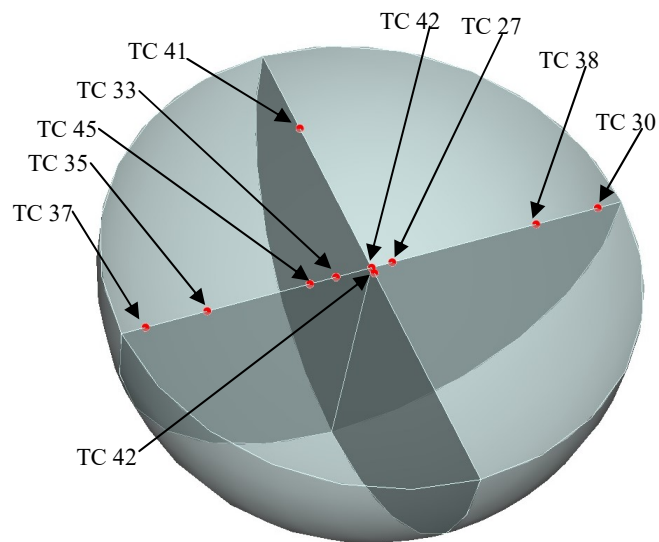

Figure A5. Thermocouples taped to the mid-plane of the top PBX 9502 hemisphere for the LT-55-2 test. The thermocouple numbering is defined in drawing number: TCLayout-Test2HE-mapped.